Parity violation in $B \to \gamma K \pi\pi$ decays

Tanim S. Islam

Under Dr. Alan J. Weinstein

California Institute of Technology

May 2000

Contents

Abstract

The short-lived B meson, which consists of a heavy bottom (b) quark and a lighter down (d) antiquark, is produced in high energy e^+e^- collisions at the CESR collider and CLEO detector. The B meson decays via the weak interaction, thus violating parity, into a K_1^* meson and a high-energy photon (γ). The K_1^* meson decays via the strong interaction into a $K^*\pi$ or $K\rho$. The presence of K^* and ρ meson resonances, with the photon, permits the observation of parity violation in $B \to K_1^*\gamma$ decays. This would constitute a unique observation of parity violation in weak decays to final states containing bosons only. An analysis of simulated data (with a perfect detector) as well as simulated data from a realistic detector (CLEO), show that the predicted maximal parity violation should be observable. We also estimate the statistical precision expected by the CLEO II and CLEO III detectors, as well as design a robust enough analysis routine that should allow for the observation of parity violation in the CLEO II and CLEO III detectors. We find that with these cuts on the data, we are able to get an expected background to noise ratio of 2:1. Furthermore, assuming negligible backgrounds, we should see a 4.6σ parity-violating effect at CLEO III for this particular decay.

1 Introduction

The study of parity and charge-parity (CP) violation is a cornerstone of particle physics, because the universe is predominated by one "handedness" of matter. The existence of top and bottom quarks to the simpler model of charm, strange, up, and down quarks was postulated (long before experimental verification of their existence) in order to allow parity violation in the Standard Model.

The observation of parity violation is a powerful probe of the weak interaction for heavy quarks. In this thesis, we are studying the measure of parity violation in neutral B decay modes. A Monte Carlo simulates the parity violating effects in the $B \to \gamma K_1^*$ decay. Preliminary analysis of generator level data focuses on all three neutral B decay modes – 1) $B^0, \overline{B^0} \to \gamma K_S^0 \pi^+ \pi^-$, and 3) $B^0, \overline{B^0} \to \gamma K_S^0 \pi^0 \pi^0$; deeper analysis focuses upon the first decay mode of the B meson, which has the highest reconstruction efficiency.

Introductory sections discuss the nature of parity violation, B physics, and the tools, such as the proper parity violating observables, used in the data analysis. Subsequent sections involve "cuts," or criteria, placed on simulated Monte Carlo events in order to be considered candidates. These cuts are performed in order to efficiently identify particles, choose proper particle

combinations, and to remove the background[1]. Final sections involve data gleaned from the "generator level"[2], which justifies the use of our analytic tools, as well as reconstruction of the simulated Monte Carlo.

2 Background Information

2.1 Parity and parity violation

All particles can be described by their position, momentum, and angular momentum. In particle decays, one speaks of a differential reaction rate $d\Gamma$ to a given configuration of daughter particles. Furthermore, if the differential rate of reaction $d\Gamma$ is the same under a transformation (often we think of sets of transformations), then that transformation is a *symmetry* transformation. In other words, the system "looks" the same when undergoing a symmetry transformation. There are four general sets of continous space-time transformations, and associated with each of the four continuous transformations are conserved quantities:

1. **rotations**: systems under which rotations are symmetry transformations conserve *angular momentum.*

[1]signal $B \to \gamma K_1^*$ events are on the order of 10^{-5} of background events such as $q\overline{q}$
[2]generator level data consists of *perfect* particle detection and identification

2. **spatial translations**: systems under which spatial translations are symmetry transformations conserve *linear momentum*.

3. **time translations**: systems under which time translations are symmetry transformations conserve *energy*.

4. **Lorentz boosts**: systems under which Lorentz boosts are symmetry transformations conserve *rest mass*. Lorentz boosts are rotations of a system in space-time.

As a further example, one can easily think of systems in which the above transformations are not symmetric. In a magnetic field, for example, particles align in a certain manner – these do not conserve angular momentum. A group of particles falling in a gravitational field do not conserve linear momentum. If these same particles moved through a time-varying potential field (such as an oscillating electric or magnetic field) which is not considered part of the system, then the energy of the system would not be conserved. Finally, noninertial systems (such as those in gravitational fields) do not conserve rest mass.

There are also three discrete transformations associated with the continuous transformations:

1. **time reversal (T)**

2. **spatial reversal (S)**: a system which is symmetric under spatial reversal conserves *parity*

3. **inversion of internal properties (i.e. charge or C)**: a system which is symmetric under this operator is its own antiparticle.

In nature, It is believed that CPT (the product charge × parity × time) is a conserved quantity. Furthermore, reactions involving the gravitational, electromagnetic, and strong forces conserve all three quantities separately. Weak decays, however, violates C and P maximally; however, the weak interaction has been observed to violate CP slightly, and is believed to violate the combination CT and PT slightly, in such a way that CPT is conserved.

The effect of these discrete transformations on particles with spin is a particularly interesting picture. All particles with spin have a certain spin polarization *along* their direction of motion. A particle which is right-handed circularly polarized has a spin component pointing along its direction of motion, or a component, with the direction of motion pointing along the +z axis, "rotating" counterclockwise; likewise, a left-handed circularly polarized particle has a spin component pointing away from its direction of motion,

or "clockwise" as seen from the +z axis. A (semiclassical) diagram should help elucidate this quantum-mechanical concept: A simple representation of

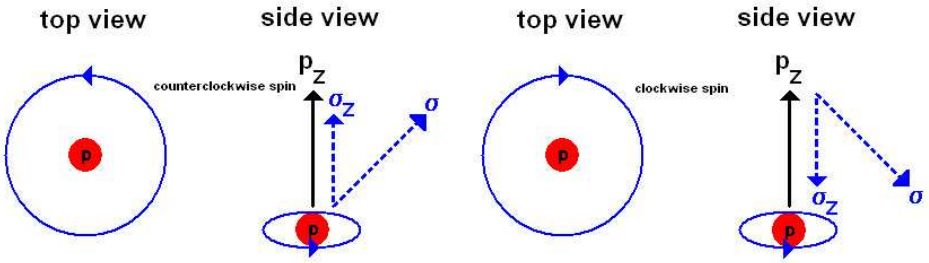

Figure 1: (left) Right-handed circularly polarized (RCP) particle. Top view represents a view in which the +z axis is along the direction of motion.

Figure 2: (right) Left-handed circularly polarized (LCP) particle. Top view represents a view in which the +z axis is along the direction of motion.

a system that violates parity is in terms of spin. Suppose that we have a spin 0 particle decaying into two spin 1 particles. One candidate here is the decay $\pi^0 \rightarrow \gamma\gamma$. *Note that the decay* $\pi^0 \rightarrow \gamma\gamma$ *conserves parity. We are using this decay only as an example.* For convenience, we show the decay in the rest frame of the π^0. The component of spin for these +1 particles along their direction of motion may be -1 (LCP), 0 (Transverse polarization, which is not possible for real photons), +1 (RCP). From conservation of linear momentum these photons move opposite each other. Angular momentum must add to zero, so both photons must be LCP or both must be RCP. Parity conservation occurs when the probability of getting a system of two LCP photons is the

same as getting two RCP photons (see figure 4).Parity violation occurs when the probability of getting both photons RCP is *different* from getting both photons LCP (see figure 3).

CP violation is a situation in which the probability distribution is different if we switch particles with antiparticles. Thus, in the case above, charge-parity violation would be observed if we get one distribution of LCP and RCP particles (from a spin 0 particle), with a parent particle, and a different distribution of LCP and RCP particles with a parent antiparticle. It is not known whether there will be significant CP violation in the $B^0 \rightarrow \gamma K\pi\pi$ decay, which is analyzed in this paper. We except parity violation to be large, but the Standard Model does not have a good prediction for the level of CP violation which we expect to see.

3 Quark Physics

3.1 Standard Model

The basic building blocks of hadrons are quarks. The Standard Model contains three families of quarks which form into mesons (i.e. quark-antiquark pairs) and baryon (three quarks): 1) up and down quarks, 2) charm and

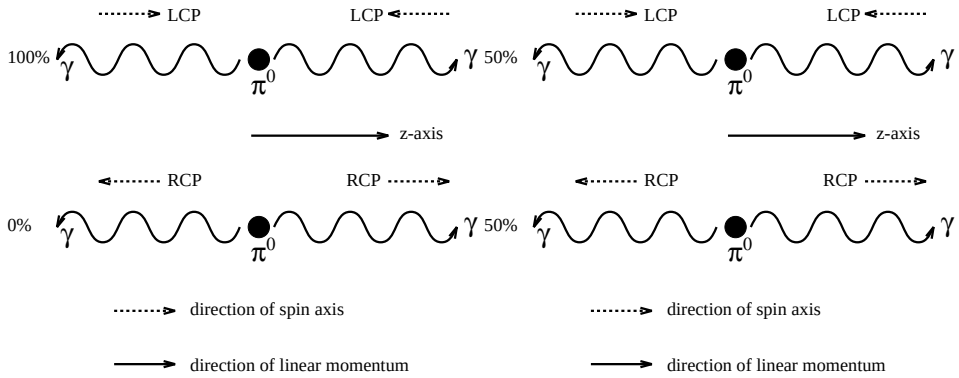

Figure 3: (left) An example of parity violation in the $\pi^0 \rightarrow \gamma\gamma$ decay. Such parity violation does not occur in nature. Note that the proportions of LCP and RCP decays are not equal. Here we have maximal parity violation.

Figure 4: (right) Parity conservation, here in the $\pi^0 \rightarrow \gamma\gamma$ decay. The proportions of LCP and RCP decays are equal.

strange quarks, and 3) top and bottom quarks. The Standard Model describes a basic universe with the following symmetries among the different particles: the first generation consists of up and down quarks (u and d) and electrons and electron antineutrinos (e and $\overline{\nu}_e$); the second generation consists of charm and strange quarks (c and s) and muons and muon antineutrinos (μ and $\overline{\mu}_\mu$); the third generation consists of top and bottom quarks (t and b) and tauons and tau antineutrinos (τ and $\overline{\nu}_\tau$). Associated with these leptons and quarks are four vector (spin-1) bosons: photon (γ), gluon (g), $W^{\pm}$, and Z^0. However well the Standard Model describes particle decay processes, it does not explain the graviton, does not predict the masses and other properties of

particles, and consequently requires a variety of parameters to explain these results.

Experimental results used to search for a better theory which includes the Standard Model would need to search for phenomenon, such as CP violation, which are not explained by the Standard Model, to determine the parameters required in the Standard Model to a higher degree of accuracy, and to observe new phenomenon predicted by the Standard Model. One example is the Higgs boson, which is theorized to give masses to the fundamental particles.

3.2 CKM Matrix

The CKM (Caribbo-Kobayashi-Maskawa) matrix is a unitary matrix which describes quark mixings via a flavor-changing charge current [1]. In the 3×3 unitary matrix, there are nine elements which describe mixings between $+2/3$ charged quarks (u, c, and t) with -1/3 charged quarks (d, s, and b). Because of its unitarity, the CKM matrix has four independent elements – three real

components and a complex phase. The CKM matrix is represented below:

$$V_{\text{CKM}} = \begin{pmatrix} V_{ud} & V_{us} & V_{ub} \\ V_{cd} & V_{cs} & V_{cb} \\ V_{td} & V_{ts} & V_{tb} \end{pmatrix} \tag{1}$$

The above describes flavor-changing mixings that may occur with quarks. *No* first-order flavor-changing neutral currents may occur, therefore we may not see decays such as $s \rightarrow dZ^0$. The following, shown below refers to the experimentally-determined magnitudes of the elements $|V_{ij}|$ of the CKM matrix [2].

$$|V_{CKM}| \approx \begin{pmatrix} 0.975 & 0.22 & 0.003 \\ 0.22 & 0.97 & 0.04 \\ 0.01 & 0.04 & 0.999 \end{pmatrix} \tag{2}$$

Actual measurements of the CKM matrix are done indirectly by experimentally determining angles in 6 "unitarity triangles," by measuring the characteristics of largely B meson decays. Any possible flavor-changing neutral currents, under the Standard Model, must occur via some second-order interaction, such as in the net decay $b \rightarrow s\gamma$, which occurs via $b \rightarrow tW^-$

and $W^- t \rightarrow s\gamma$ (see figure 5 and equation 8). We can see this particular decay because the decay chains $b \rightarrow u \rightarrow s$ and $b \rightarrow c \rightarrow s$ are "suppressed." First, from equations 1 and 2, $|V_{bt}V_{ts}^*| >> |V_{bu}V_{us}^*|$. Second, although $|V_{bt}V_{ts}^*| \approx |V_{bc}V_{cs}^*|$, and $\mathcal{B}(b \rightarrow s\gamma)/\mathcal{B}(b \rightarrow c) \approx 10^{-4}$, $b \rightarrow c$ occur with a high enough frequency that $b \rightarrow s\gamma$ decays may also be observed.

CP violation will be most apparently manifest by complex phases in the CKM matrix with nonzero imaginary elements – that is, mixing elements among quarks will be different from that among antiquarks. In fact, in order to bring CP violation into the CKM matrix, Kobayashi and Matsuko postulated an extra dimension in the 2×2 matrix (corresponding to the two generations of quarks and leptons known at that time). This follows from the fact that a 2×2 unitary matrix would only be real, thus no parity violation.

B mesons provide a useful test of the parity and possibly CP violating portions of the Standard Model, as well as possible extensions to the Standard Model, due to the fact that B mesons consist of one third generation quark. Furthermore, B mesons also decay through an immense number of different decay channels, many of which provide tests of various aspects of the Standard Model and heavy quark physics.

4 B physics

4.1 $B^0, \overline{B^0}$ parity violation

Parity violation has been observed in inclusive semileptonic B meson decays [5] and exclusive semileptonic B meson decays [6]. Parity violation is also expected to be just as strong in B hadronic and electromagnetic decays. Here we outline a method for measuring the degree of parity violation in the final state of the $\overline{B^0} \to \overline{K_1^*}\gamma$ decay.

The photon is expected to be strongly polarized due to parity violation in the weak interaction. However, we cannot measure the polarization of the photon (i.e. its energy is too high), and all we have are the momenta of the final decay products. The simplest parity-violating observable that we can measure is some observable constructed out of the triple product $\mathbf{p}_\gamma \cdot \mathbf{p}_K \times \mathbf{p}_{\pi_1}$, where $\mathbf{p}_{\pi_1}$ is the pion such that $m_{K\pi_1} > m_{K\pi_2}$ (see figure 8). Thus, this parity-violating observable, $\cos\theta_H$, or the cosine helicity angle, is defined as the following:

$$\cos\theta_H = \hat{\mathbf{p}}_\gamma \cdot \text{norm}(\mathbf{p}_K \times \mathbf{p}_{\pi_1}) \tag{3}$$

$$\cos\theta_H = \frac{p_\gamma \cdot (\mathbf{p}_K \times \mathbf{p}_{\pi_1})}{|p_\gamma|\,|\mathbf{p}_K \times \mathbf{p}_{\pi_1}|} \tag{4}$$

Where all momenta are taken in the K_1 rest frame.

However, this does not necessarily produce a parity-violating observable, although we have resolved the ambiguity of which orientation to measure this triple product. The physics of the decay must be able to distinguish between the +1 and -1 helicities of the $\overline{K_1^*}$. This can only occur in a small class of decays, such as $a_1 \rightarrow 3\pi$ and $K_1 \rightarrow K\pi\pi$ because these decays proceed via two or more amplitudes which interfere. This interference sign flips under parity, allowing one to distinguish between +1 and -1 helicities. This explanation is covered in greater detail in the section "Parity-Violating Observations."

Although the $\overline{B^0} \rightarrow \overline{K_1^*}\gamma$ decay has not been observed, the efficiency for reconstructing the final state is relatively high. There will be hundreds of events in CLEO III, which will be accumulated over the next few years, allowing this statistical analysis.

4.2 Calculation of the PV decay rate in $\overline{B^0} \rightarrow \gamma\overline{K_1^*}$

We are splitting the decay $B \rightarrow \gamma K\pi\pi$ into two independent portions: 1) $\overline{B^0} \rightarrow \gamma K_1^*$, which we analyze in this section, and 2) $\overline{K_1^*} \rightarrow K\rho, K^*\pi$. As stated in the abstract and shown in figure 5, the $\overline{B^0}$ consists of a b and $\overline{d}$

quarks. The decay $\overline{B^0} \rightarrow \gamma\overline{K_1^*}$, by means of $b \rightarrow s\gamma$, occurs over 10^{-25} seconds over a distance of 10^{-18} meters; the decay of the $\overline{K_1^*}$ occurs over a 10^{-23} seconds over a distance of 10^{-16} meters. Therefore we may consider the $\overline{B^0}$ decay as independent of the $\overline{K_1^*}$.

The decay we are studying can be described using relativistic quantum field theory. One may write out down the expression for the decay rate Γ, fully differential in all the momenta of all the particles. The differential decay rate is given by the following equation:

$$d\Gamma = \frac{1}{2m_B}|\mathcal{M}|^2 dPS_2 \tag{5}$$

Where m_B is the mass of the $\overline{B^0}$ meson, dPS_2 is a differential element of the two-particle ($\gamma, \overline{K_1^*}$ phase space, and $\mathcal{M}$ is the quantum mechanical matrix which describes the decay $\overline{B^0} \rightarrow \gamma\overline{K_1^*}$. The two dimensional phase space is given by the following:

$$dPS_2 = \frac{1}{8\pi}\left(\frac{2p_\gamma}{m_B}\right) = \frac{m_B^2 - m_{K_1}^2}{8\pi m_B^2} \tag{6}$$

Where m_{K_1} is the mass of the $\overline{K_1^*}$ meson. Figure 5 is a sketch of the $\overline{B^0} \rightarrow \gamma\overline{K_1^*}$ decay. Here is the form of the quantum mechanical decay matrix, which

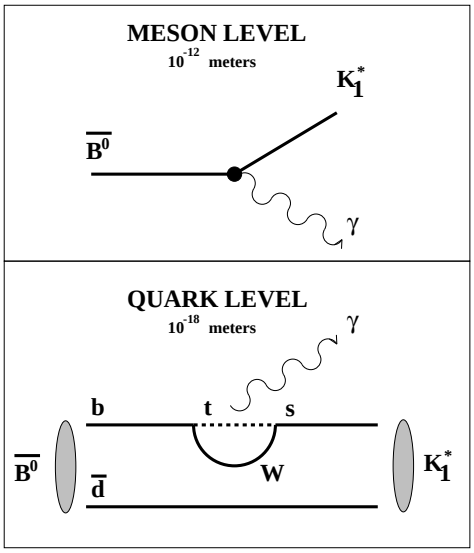

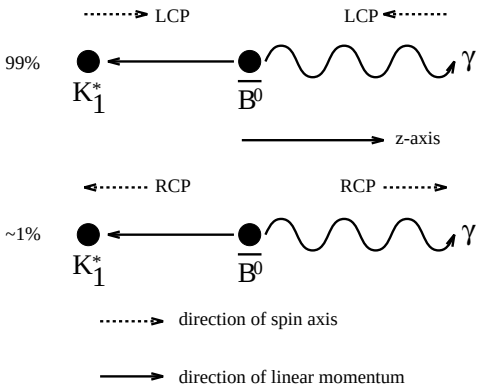

Figure 5: (left) The decay $\overline{B^0} \to \overline{K_1^*}\gamma$ at the meson and the quark levels. The decay $b \to s\gamma$ proceeds via an expected parity-violating "penguin" decay.

Figure 6: (right) Expected parity violations in the $\overline{B^0} \to \overline{K_1^*}\gamma$ decay. Parity conservation occurs when the probability for both decay processes, as shown above, are equal. Parity violation occurs when the probabilities of both processes are unequal.

contains all the weak-interaction physics in this decay:

$$\mathcal{M} = G_2 \varepsilon_\gamma^\mu \left\langle \overline{K_1^*} | \hat{J}_\mu | \overline{B^0} \right\rangle \tag{7}$$

Where ε_γ^μ is the photon polarization and G_2 is the weak radiative penguin coupling:

$$G_2 = \frac{G_F}{\sqrt{2}} \frac{e^2}{4\pi^2} V_{bt} V_{ts}^* \tilde{F}_2(m_t^2/m_W^2) \tag{8}$$

$\tilde{F}_2$ is a known function of the top quark mass that characterizes these penguin loops [7].

$\hat{J}_\mu$ describes a magnetic transition between the $\overline{B^0}$ and the $\overline{K_1^*}$; it must include the polarization vectors ε_{K_1} and ε_γ but also the 4-vectors P_{K_1} and P_γ. It consists of both polar and axial vectors in this nontrivial combination:

$$\begin{aligned}\varepsilon_\gamma^\mu \left\langle \overline{K_1^*}|\hat{J}_\mu|\overline{B^0}\right\rangle = i\epsilon_{\mu\alpha\beta\delta}\varepsilon_\gamma^\mu \varepsilon_{K_1}^\alpha P_\gamma^\beta P_{K_1}^\delta T_1(0) m_B h + \\ [(\varepsilon_\gamma \cdot \varepsilon_{K_1})(P_\gamma \cdot P_{K_1}) - (\varepsilon_\gamma \cdot P_{K_1})(\varepsilon_{K_1} \cdot P_\gamma)] T_2(0) m_B\end{aligned} \tag{9}$$

T_1 is the polar vector and T_2 is the axial vector hadronic form- factors evaluated at the 4-momentum transfer $q^2 = (P_B - P_{K_1})^2 = P_\gamma^2 = 0$. $h = \pm 1$ for $V \mp A$ currents, and in the Standard Model, $h = 1$, and m_B is the B meson mass, inserted to make $T_{1,2}$ unitless. The above is the only nontrivial combinations of four independent 4-vectors, since $P_{K_1} \cdot \varepsilon_{K_1} = P_\gamma \cdot \varepsilon_\gamma = 0$ for these divergenceless currents.

Now we evaluate the above in the $\overline{K_1^*}$ rest frame, taking the photon direction to be along the $\hat{z}$ axis. The components of the four-momenta in

this frame become:

$$\varepsilon_\gamma = \left(0, \pm\frac{1}{\sqrt{2}}, -\frac{i}{\sqrt{2}}, 0\right) \tag{10}$$

$$\varepsilon_{K_1} = \left(0, \mp\frac{1}{\sqrt{2}}, -\frac{i}{\sqrt{2}}, 0\right) \tag{11}$$

$$P_\gamma = (E_\gamma, 0, 0, E_\gamma) \tag{12}$$

$$P_{K_1} = (m_{K_1}, 0, 0, 0) \tag{13}$$

Where the + sign corresponds to RCP photon and - sign corresponds to LCP photon; $E_\gamma = (m_B^2 - m_{K_1}^2)/(2m_{K_1})$. Note that $\varepsilon_\gamma \cdot P_{K_1} = \varepsilon_{K_1} \cdot P_\gamma = 0$. Note that $\varepsilon_\gamma \cdot \varepsilon_{K_1} = 1$ and $P_\gamma \cdot P_{K_1} = E_\gamma m_{K_1} = \frac{1}{2}(m_B^2 - m_{K_1}^2)$. Evaluating the first term of equation 9, we get $m_B E_\gamma m_{K_1} T_1$.

The coefficient contributing to T_2 may be found by noting that the fourth rank Levi-Civita tensor $\epsilon_{\mu\alpha\beta\delta}$ is antisymmetric under the interchange of its indices. Thus, it is nonzero only when all its indices are different. We may

rewrite the coefficient associated with T_1 as the following:

$$\epsilon_{\mu\alpha\beta\delta}\varepsilon^{\mu}_{\gamma}\varepsilon^{\alpha}_{K_1}P^{\beta}_{\gamma}P^{\delta}_{K_1} = \epsilon_{xyzt}\varepsilon^{x}_{\gamma}\varepsilon^{y}_{K_1}P^{z}_{\gamma}P^{t}_{K_1} + \epsilon_{yxzt}\varepsilon^{y}_{\gamma}\varepsilon^{x}_{K_1}P^{z}_{\gamma}P^{t}_{K_1} \tag{14}$$

$$= \left(\pm\frac{1}{\sqrt{2}}\right)\left(-\frac{i}{\sqrt{2}}\right)E_{\gamma}m_{K_1} - \left(\mp\frac{1}{\sqrt{2}}\right)\left(-\frac{i}{\sqrt{2}}\right)E_{\gamma}m_{K_1} \tag{15}$$

$$= \mp iE_{\gamma}m_{K_1} \tag{16}$$

The two nonzero terms in the decay matrix M have equal magnitude, and thus:

$$\mathcal{M} = e\frac{G_2}{\sqrt{2}}V_{bt}V^{*}_{ts}\tilde{F}_2(m_t^2/m_W^2)\frac{m_B^2 - m_{K_1}^2}{2}[\pm hT_1(0) + T_2(0)]m_B \tag{17}$$

And the decay rate Γ, the decay rate for RCP photons $d\Gamma_+$, and the decay rate for LCP $d\Gamma_-$ are given by the following equations:

$$d\Gamma_{\pm} = \frac{G_F^2\alpha|V_{bt}V^{*}_{ts}|^2m_B^5}{16\pi}|\pm hT_1(0) + T_2(0)|^2 \tag{18}$$

$$\Gamma = \frac{G_F^2\alpha|V_{bt}V^{*}_{ts}|^2m_B^5}{8\pi}[|T_1|^2 + |T_2|^2] \tag{19}$$

Where we have summed over both helicities in equation 19. Here, the parity-

violating asymmetry is given by:

$$\mathcal{A}_{\gamma K_1} = \frac{d\Gamma_+ - d\Gamma_-}{d\Gamma_+ + d\Gamma_-} = \frac{2hT_1T_2}{|T_1|^2 + |T_2|^2} = \frac{2hT_2/T_1}{1 + |T_2/T_1|^2} \tag{20}$$

It is estimated that for $B \to \gamma K^*(892)$, $T_1 \approx T_2 \approx 0.115$, which leads to *maximal parity violation* and a completely polarized photon [8]. It is assumed that the symmetry is also large for the decay $B \to \gamma K_1$.

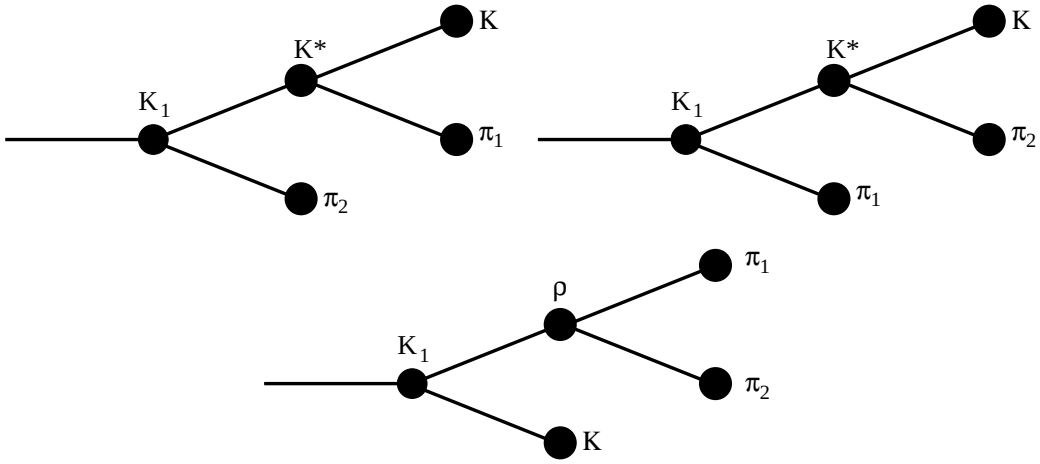

Figure 7: various resonances in the decay $K_1 \to K\pi\pi$. The first decay is $K_1 \to K^*\pi_2$, $K^* \to K\pi_1$. The second decay is $K_1 \to K^*\pi_1$, $K^* \to K\pi_2$. The third decay resonance is $K_1 \to K\rho$, $\rho \to \pi_1\pi_2$. The more resonances there are, the larger the number of interference between the resonances, and there is expected to be a larger parity-violating effect.

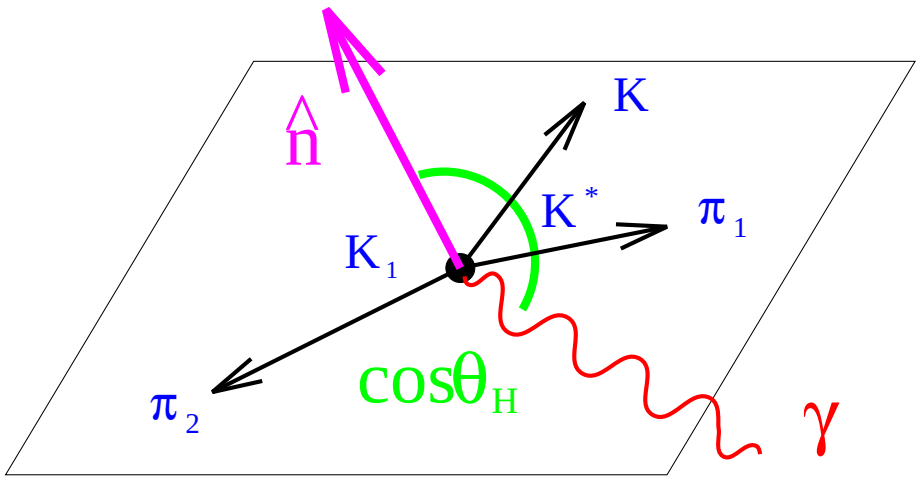

Figure 8: The K_1^* decay plane. All 4-momenta are taken in the rest frame of the K_1^*. Note also that the normal to the plane is defined as the normalized cross product of the kaon three-momentum with the "faster" pion 3-momentum.

4.3 CP violation

If T_2/T_1 were complex, with a weak phase which flips sign under parity, then the parity-violating asymmetry $\mathcal{A}_{\gamma K_1}$ will be different for B than for $\overline{B}$. The penguin decay should contribute to both the polar vector V and axial vector A portions of the current with amplitudes T_1 and T_2 with only strong interaction phases, not weak interaction phases. The Standard Model does not predict CP violation in this decay. However, any CP violation we see would signal beyond-Standard Model physics.

A simple test of CP violation in this $B \to \gamma K \pi\pi$ decay can be found by the following. First, $B^0 \to \gamma K^- \pi^+ \pi^0$ only (i.e. not its charge-conjugated

combination, or $\gamma K^+\pi^-\pi^0$), while $\overline{B^0} \rightarrow \gamma K^+\pi^-\pi^0$. Supposing we have maximal parity violation, and we measure some parity-violating observable. If we measure a different value for the observable for $B^0 \rightarrow \gamma K^-\pi^+\pi^0$ decays relative to $\overline{B^0} \rightarrow \gamma K^+\pi^-\pi^0$ decays, then we observe parity violation – a signal of physics beyond the Standard Model. CP violation necessarily does not occur in the other two neutral B decay modes – $B^0, \overline{B^0} \rightarrow \gamma K^0_S\pi^+\pi^-$, $B^0, \overline{B^0} \rightarrow \gamma K^0_S\pi^0\pi^0$.

4.4 Parity-Violating Observations

The derivation of a parity-violating observable, as defined in equations 3 and 4 are borrowed directly from Weinstein's derivation in "Parity and CP Violation in $B \rightarrow \gamma K\pi\pi$."

There is no way to measure the polarization of the photon, so we must measure the equal (but opposite) polarization of the K_1 via its decay products. One cannot distinguish +1 and -1 helicities in $V \rightarrow PP$ decays, such as $K_1 \rightarrow K^*\pi$; the decay angle is $\cos^2\theta$ in this case.

The decay rate for a polarized $K_1 \rightarrow K\pi\pi$ is given by the following

expression:

$$d\Gamma(K_1 \to K\pi\pi) = \frac{1}{2m_{K_1}} \left| g_{K_1} g_{K\pi\pi} \mathcal{E}^{\mu}_{K_1} J_{K_1\mu} \right| dPS_3 \tag{21}$$

Where $g_{K_1} g_{K\pi\pi}$ is the roughly constant strong mesonic coupling, and $J^{\mu}_{K_1}$ is the decay current, given below. The three-particle phase space is given by:

$$dPS_3 = \frac{1}{(2\pi)^3 16 m^2_{K_1}} \, dm^2_{K\pi} \, dm^2_{\pi\pi} \frac{d\cos\theta_H}{2} \frac{d\alpha}{2\pi} \frac{d\phi}{2\pi} \tag{22}$$

Where $\cos\theta_H$ is the cosine of the helicity angle, defined as in equations 3 and 4. Furthermore, α and ϕ are, for this problem, uninteresting azimuthal angles defined among the decay products. If we take $\mathcal{E}^{\mu}_{K_1} = A_+ \mathcal{E}^{\mu}_{+} + A_- \mathcal{E}^{\mu}_{-} + A_0 \mathcal{E}^{\mu}_{0}$, then we get a rate of the following form:

$$\frac{d\Gamma}{d\cos\theta_H} \propto \left| H_+ \frac{1+\cos\theta_H}{2} + H_0 \sin\theta_H + H_- \frac{1-\cos\theta_H}{2} \right|^2 \tag{23}$$

where H_+, H_-, H_0 are helicity form factors that can be related to A_+, A_-, A_0 but that also depend on $J^{\mu}_{K_1}$. If $H_+ \neq H_-$ then parity is evidently violated.

In our case, if $T_1 = T_2$, then parity is maximally violated and the photon is completely polarized; by helicity conservation so is the K_1, so A_- is the

only nonzero term. This does not necessarily lead to H_- being the only nonzero helicity form factor. As mentioned above, there is an ambiguity in the direction of the normal to the $K\pi\pi$ decay plane, which results in an ambiguity in the sign of $\cos\theta_H$.

However, this decay proceeds via an intermediate K^* resonance, and there are two amplitudes that contribute. For example, for $D^0 \to K^+\pi^-\pi^0$, the amplitudes are for $D^0 \to K^{*+}\pi^-$ and $D^0 \to K^{*0}\pi^0$. There is a region in the Dalitz plot where these two components interfere (see figure 12). The interference term is of opposite parity than the direct terms, leading to a non-zero expectation value for the helicity angle $< \cos\theta_H >$. This expectation value should be proportional to the parity-violating asymmetry $\mathcal{A}_{\gamma K_1} = (d\Gamma_+ - d\Gamma_-)/(d\Gamma_+ + d\Gamma_-)$.

We analyze this by replacing $\mathcal{E}_{K_1}$ (which cannot be measured directly) with the $K_1 \to K\pi\pi$ decay current (Fig. 7), which plays the role of $\mathcal{E}_{K_1}$ in the Feynman calculus when the K_1 decays. This current must depend only on the daughter particle momenta, and, like $\mathcal{E}_{K_1}$, must be transverse to P_{K_1}.

This uniquely determines the Lorentz structure of the current:

$$J^{\mu}(K_1 \to K\pi\pi) = T^{\mu\nu}(K_1)\,[F_1(m^2_{K\pi_1})T_{\nu\alpha}(K\pi_1)(P_K - P_{\pi_1})^{\alpha} + F_2(m^2_{K\pi_2})T_{\nu\alpha}(K\pi_2)(P_K - P_{\pi_2})^{\alpha} + F_3(m^2_{\pi_1\pi_2})T_{\nu\alpha}(\pi_1\pi_2)(P_{\pi_1} - P_{\pi_2})^{\alpha}\,] \tag{24}$$

where the (axial)vector transversality projectors are $T^{\nu\alpha} = -g^{\nu\alpha} + P^{\nu}P^{\alpha}/P^2$. F_1, F_2, and F_3 are more hadronic form-factors These, however, are given by the resonance dominance model; they are simply Breit-Wigners for the K^* (F_1, F_2) or the ρ meson (F_3). By isospin-Bose symmetry, F_1 and F_2 should have equal normalizations at equal values of their arguments. Thus, they are given by:

$$F_{1,2} = \frac{C_{K^*}}{m^2_{K^*} - m^2_{K\pi_{1,2}} - i m_{K\pi_{1,2}}\Gamma_{K^*}}, \tag{25}$$

$$F_3 = \frac{C_{\rho}}{m^2_{\rho} - m^2_{\pi\pi} - i m_{\pi\pi}\Gamma_{\rho}} \tag{26}$$

The form factors are complex (strong interaction phases). The values of C_{K^*} and C_{ρ} can be determined from the K_1 branching fractions (best determined by CLEO [3]). Note that there are two K_1 mesons ($K_1(1270)$ and $K_1(1400)$) with different branching fractions to $K^*\pi$ and $K\rho$ (and other modes). This

is a subtlety which does not concern us too much at this level of analysis.

This current will appear twice in $|M|^2$, and the interference term will have both real and imaginary parts (maximum in the vicinity $m^2(K\pi_1) \approx m^2(K\pi_2) \approx m^2(K^*)$). The imaginary part will be odd under the exchange $\pi_1 \leftrightarrow \pi_2$ and thus will be parity-odd. This permits the distinction between helicity $+1$ and -1 decay amplitudes in the K_1 decay.

Note also that there also exists a (small) Wess-Zumino term of the form $\epsilon_{\mu\nu\alpha\beta} P_K^\nu P_{\pi_1}^\alpha P_{\pi_2}^\beta$ which has opposite parity from the $F_{1,2,3}$ terms, providing yet another non-zero effect the parity-violating measurables. It is expected to be a small contribution, and is neglected here, but it is an important source of systematic uncertainty.

5 Data Analysis

5.1 Asymmetry statistical analysis

The simplest statistical test involves counting the number of events, out of the total number N, in which $\cos\theta_H > 0$, labeled N_+, and the number of events out of N in which $\cos\theta_H < 0$, labeled N_-. N_+/N is an estimate of $d\Gamma_+/\Gamma$, and N_-/N is an estimate of $d\Gamma_-/\Gamma$. Thus, for each combination of

polar and axial vector form factors T_1 and T_2, there is the following parity-violating *asymmetry observable*, which should scale linearly with the parity-violating parameter (see align 20):

$$\mathcal{A}_{\gamma K_1} = \frac{N_+ - N_-}{N_+ + N_-} \tag{27}$$

The errors on the quantities N_+ and N_- are given by

$$\sigma_+ = \sqrt{N_+} \tag{28}$$

$$\sigma_- = \sqrt{N_-} \tag{29}$$

The error on the quantity $\mathcal{A}$ is then

$$\sigma_{\mathcal{A}} = \frac{2N_+N_-}{(N_+ + N_-)^2}\sqrt{\frac{\sigma_+^2}{N_+^2} + \frac{\sigma_-^2}{N_-^2}} = \frac{2N_+N_-}{(N_+ + N_-)^2}\sqrt{\frac{1}{N_+} + \frac{1}{N_-}} \tag{30}$$

5.2 Regression fit analysis

For each value of the parity violating parameter, we fit the distribution of the cosine of the helicity angle to a quadratic of the following form, where $x = \cos\theta_H$ and $\mathcal{N}$ is a normalization constant, equal to twice the number of

events times the bin width:

$$R(x) = \mathcal{N}\left(\frac{a}{2a + 2/3c} + \mathcal{P}x + \frac{c}{2a + 2/3c}x^2\right) \tag{31}$$

We modified T_1 from 0 to 1 so that the independent parity-violating parameter $2T_1T_2/(T_1^2 + T_2^2)$ went from 0 to 1 in steps of 0.1. We then constructed this parity-violating parameter and its error:

$$F = \frac{\int_0^1 R(x)\,dx - \int_{-1}^0 R(x)\,dx}{\int_{-1}^1 R(x)\,dx} = \mathcal{P} \tag{32}$$

The beauty of this method is that one does not require the correlation matrix between the three variables a, c, and $\mathcal{P}$ in order to determine the parity-violating parameter; the parity-violating parameter is merely $\mathcal{P}$, whose errors can be quickly calculated using the MN_FIT software package. In addition, we are interested only in the parameters $\mathcal{N}$ and $\mathcal{B}$; The parameter a was fixed in order to reduce the statistical error in the fit, which in turn reduces the correlation between the "irrelevant" parameters a and c and the relevant parameters $\mathcal{N}$ and $\mathcal{B}$, and hence their errors, thus $\sigma_F = \sigma_{\mathcal{P}}$.

5.3 Efficiency

The method of analysis described with the Monte Carlo data applies here. The hadronic form factor T_1 is modified from 0 to 1, with $T_2 = 0.115$, in such a manner that the parity-violating parameter $2T_1T_2/(T_1^2 + T_2^2)$ ranges from 0 to 1 in steps of 0.1. To get a model for the efficiency, let N be the number of events, A be the number of mode reconstructions, and $N^A = N - A$ be the number of non-reconstructed events. Then we have the following relation, considering in the limiting case of large N that N^A and A behave independently and according to Poisson statistics:

$$\epsilon = \frac{A}{A + N^A} \tag{33}$$

$$\sigma_\epsilon = \sqrt{\left(\frac{\partial \epsilon}{\partial A}\right)^2 \sigma_A^2 + \left(\frac{\partial \epsilon}{\partial N^A}\right)^2 \sigma_{N^A}^2} \tag{34}$$

Note the following two relations:

$$\frac{\partial \epsilon}{\partial A} = \frac{\partial}{\partial A}\left(1 - \frac{B}{A + N^A}\right) = \frac{B}{(A + N^A)^2} = \epsilon \frac{N^A/A}{N} \tag{35}$$

$$\frac{\partial \epsilon}{\partial N^A} = \frac{\partial}{\partial N^A}\left(\frac{A}{A + N^A}\right) = -\frac{A}{(A + N^A)^2} = -\epsilon \frac{1}{N} \tag{36}$$

Simplifying 34, we get the following relation, since $\sigma_A = \sqrt{A}$ and $\sigma_{N^A} = \sqrt{N^A}$:

$$\sigma_\epsilon = \epsilon\sqrt{\frac{N^{A^2}/A^2}{A^2}\sigma_A^2 + \frac{1}{N^2}\sigma_{N^A}^2} = \epsilon\sqrt{\frac{N^{A^2}/A}{N^2} + \frac{1 - A/N}{N}} \tag{37}$$

Note that $A = N\epsilon$ and $B = N(1-\epsilon)$. Then we have

$$\sigma_\epsilon = \epsilon\sqrt{\frac{(1-\epsilon)^2}{\epsilon N} + \frac{1-\epsilon}{N}} = \epsilon\sqrt{\frac{(1-\epsilon)(1-\epsilon+\epsilon)}{\epsilon N}} = \sqrt{\frac{\epsilon(1-\epsilon)}{N}} \tag{38}$$

6 Generator Level Analysis

6.1 Introduction

The Monte Carlo simulates the particle decays and the particles' momenta according to the following: first, conservation of momenta and energy; second, the model (see section 4) that describes the parity violating $B \to \gamma K_1^*$ decay, and the resonant structure of the K_1^* decay; and third, the specific decay (such as $\overline{B^0} \to K^+\pi^-\pi^0$). The code for this parity violating Monte Carlo was written by Dr. Alan Weinstein.

In the Monte Carlo simulation, the K_S^0 has a lifetime ($\approx 8.9\times10^{-11}$) [9] too

short to exit the drift chamber, while the K_L^0, with its much longer lifetime ($5.17 \pm 0.14 \times 10^{-8}$ s) [9], often leaves the detector before decaying. The K_S^0 can be detected with a reasonable ($\approx 20\%$) efficiency by reconstruction from its daughter particles, while the K_L^0 is much more difficult to detect. In data analysis using a simulated CLEO detector, one usually searches for K_S^0 and not K_L^0.

The Monte Carlo simulates the decays $\overline{B^0} \rightarrow \overline{K_1^*}\gamma$, $\overline{K_1^*} \rightarrow K^*\pi$ (two combinations, one for each pion), and $\overline{K_1^*} \rightarrow K\rho$ (one combination). The final combinations analyzed by the Monte Carlo are $\overline{B^0} \rightarrow \gamma K^+\pi^-\pi^0$, $\overline{B^0} \rightarrow \gamma K_S^0\pi^+\pi^-$, and $\overline{B^0} \rightarrow \gamma K_S^0\pi^0\pi^0$.

Generator level data contains particle ID and ancestry for all particles produced in an event. The feasibility of the parity-violating model is most easily tested through the data taken at the generator level for the following obvious reasons; 1) the efficiency and resolution for reconstruction are perfect since particle identification and momenta are perfect, and 2) there are backgrounds (i.e. $B\overline{B}$ or $q\overline{q}$. However, a *reconstruction* of the simulated Monte Carlo has imperfect efficiency, a finite resolution, and contains background.

6.2 Kinematic Plots of B Decay at the Generator Level

Attached to these figures are plots of the B decay's kinematic quantities (momenta, energies, angles, and invariant masses) at the generator level, or the level where we have perfect particle identification. The mass of the particle combinations $K\pi$ and $\pi\pi$ are peaked about the resonant masses of the particles. The Dalitz plots also show evidence of the resonance K^* and ρ. All these plots are taken with only this simulated decay chain $B^0, \overline{B^0} \rightarrow \gamma K^+\pi^-\pi^0$ (see figures 10, 11, 9, 12). Plots generated from the other two neutral B decay chains, although not shown, are identical to these kinematic plots, within statistical fluctuations.

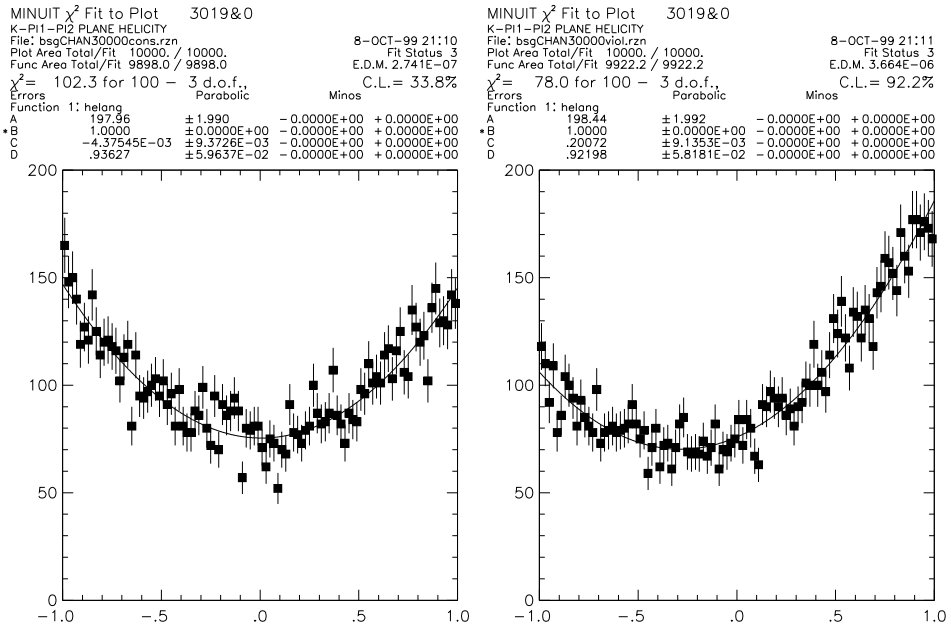

Figure 9: The distribution of the parity-violating triple product, $\cos\theta_H$ (a) where the hadronic form-factor $T_1 = 0$ (identical to $T_2 = 0$) (b) where $T_1 = T_2 \neq 0$. This is taken from generator level data for the $\overline{B^0} \to \gamma K^+\pi^-\pi^0$ decay.

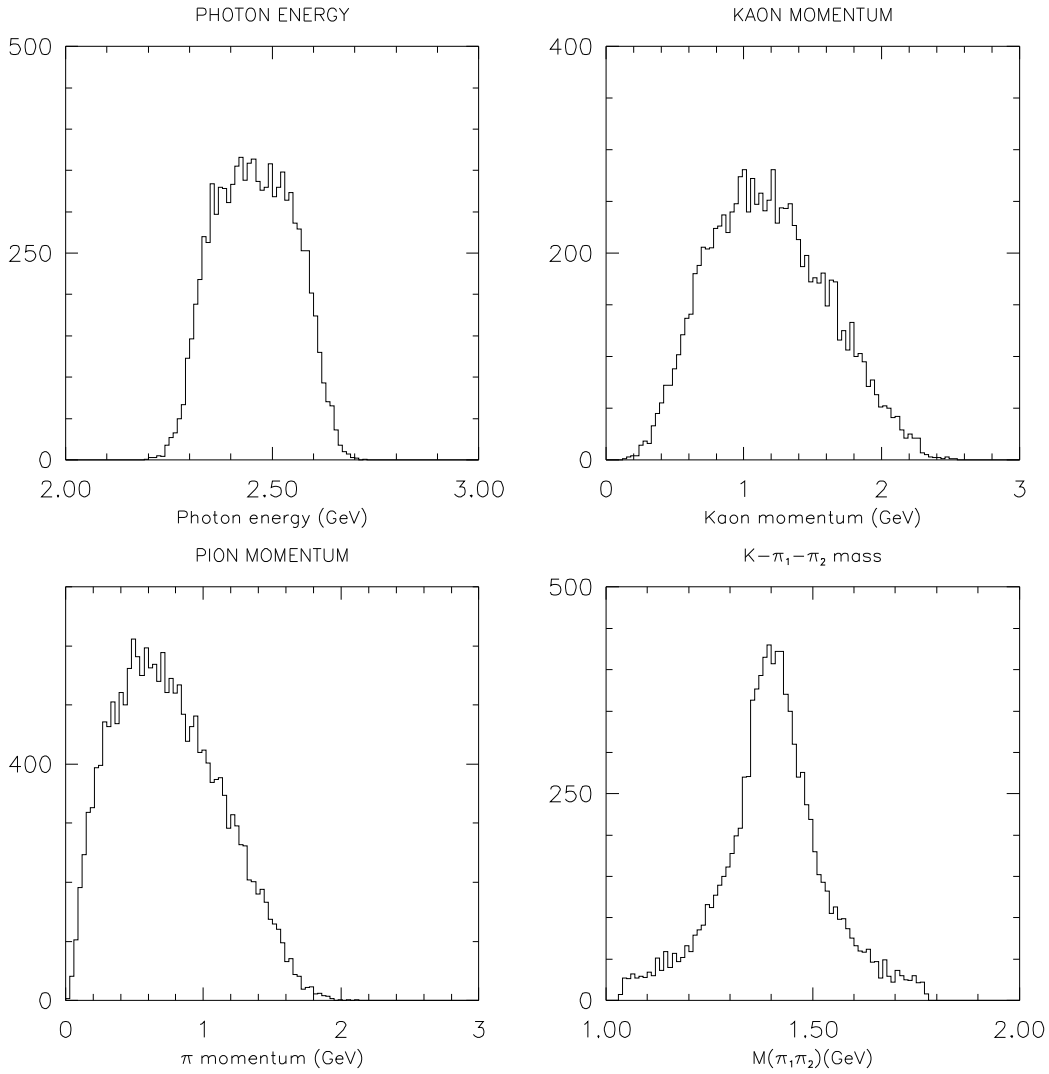

Figure 10: Dynamics for the decay $B \to \gamma K_1^*, K_1^* \to K\pi\pi$ via $K^*\pi$ and $K\rho$, for Monte Carlo level data: (a) photon energy spectrum, (b) kaon momentum spectrum, (c) pion momentum spectrum, (d) $K\pi\pi$ mass spectrum. This is taken from generator level data for the $\overline{B^0} \to \gamma K^+\pi^-\pi^0$ decay.

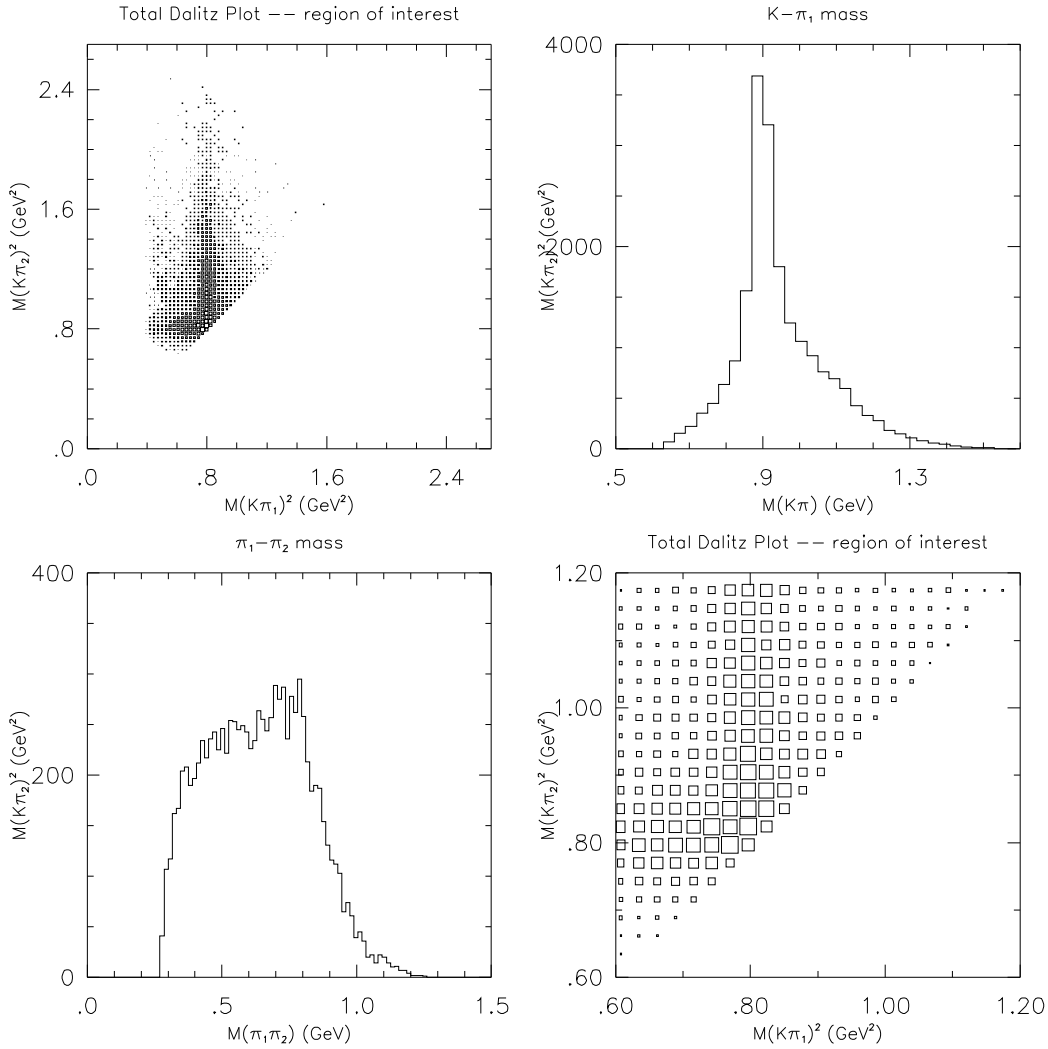

Figure 11: More dynamics for the decay $B \to \gamma K_1^*$, $K_1^* \to K\pi\pi$ via $K^*\pi$ or $K\rho$, for MC data. (a) The folded Dalitz plot, with $m_{K\pi_{high}}$ vs $m_{K\pi_{low}}$ (b) $K\pi$ mass spectrum (two entries per event). (c) $\pi\pi$ mass spectrum. (d) The folded Dalitz plot, with $m_{K\pi_{high}}$ vs $m_{K\pi_{low}}$ in the K^* mass region. This is taken from MC level data for the $\overline{B^0} \to \gamma K^+\pi^-\pi^0$ decay.

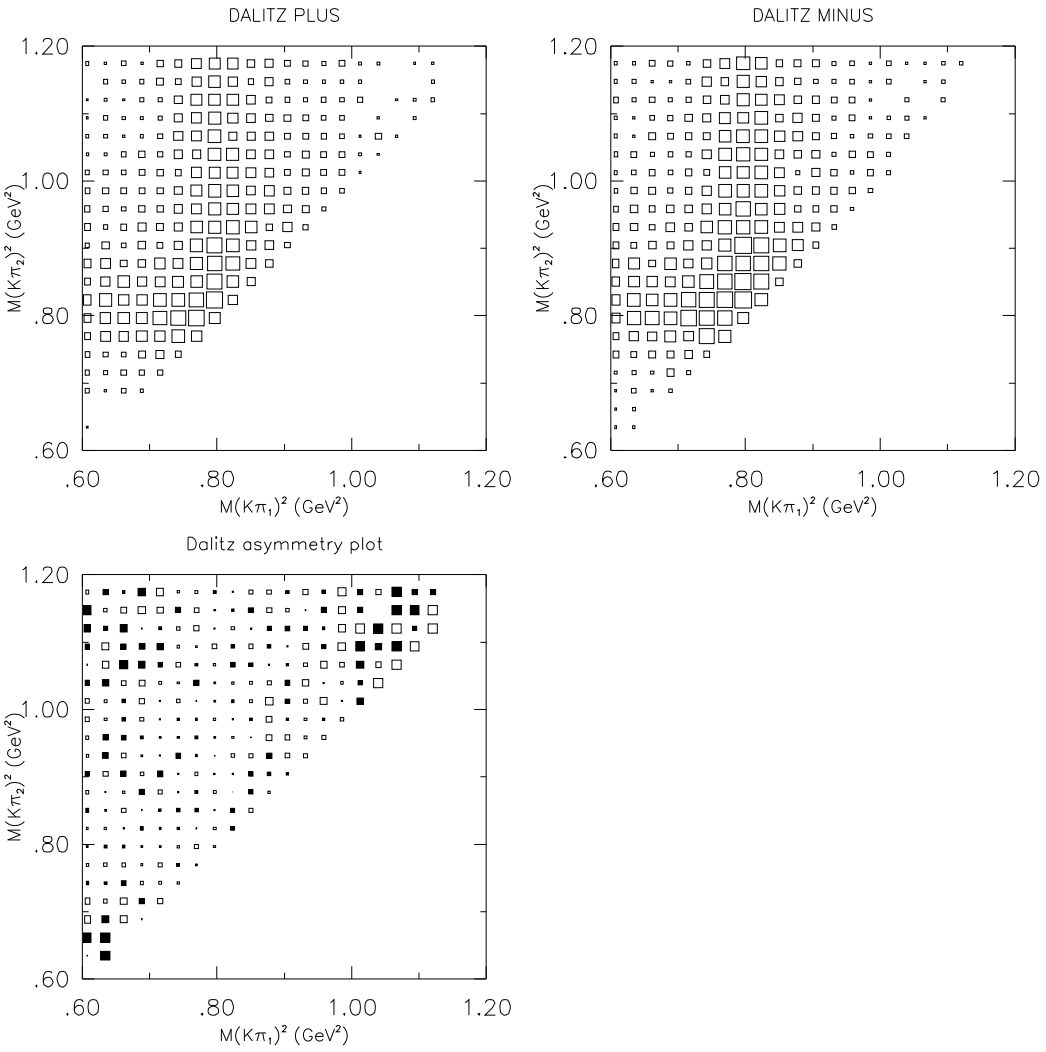

Figure 12: Folded Dalitz plot for (a) events in which the parity-violating triple product is greater than zero, (b) where the product is less than zero, and (c) asymmetry plot $((a-b)/(a+b))$, after normalization of plots to equal areas. Note that the interference effect is strongest at the K^* mass in both diagrams. This is taken from MC level data for the $\overline{B^0} \to \gamma K^+\pi^-\pi^0$ decay.

6.3 Statistical Analysis of Generator-Level Data

Shown below are the plots of the asymmetry observable $\mathcal{A}$ and the parity-violating observable $\mathcal{P}$, as defined above, for the three decay modes of the neutral B, $B^0, \overline{B^0} \to \gamma K^{\pm}\pi^{\mp}\pi^0$, $B^0, \overline{B^0} \to \gamma K^0_S\pi^+\pi^-$, and $B^0, \overline{B^0} \to \gamma K^0_S\pi^0\pi^0$ (for which no observable parity violation is expected, since the decay products are all CP eigenstates π^0, K^0_S). Furthermore, table 1 gives the following information for all three decay chains: 1) $\mathcal{A}$ and $\mathcal{P}$ with statistical errors, and 2) the number of standard deviations these values, at maximal parity violation, are from parity conserving values of $\mathcal{A} = 0$ and $\mathcal{P} = 0$.

As a test of our ability to measure the parity-violating parameter, $2T_1T_2/(T_1^2+T_2^2)$ for observed values of the asymmetry $\mathcal{A}$ and $\mathcal{P}$, for each Monte Carlo sample (usually 11) in each neutral B decay mode, we vary the value of the parity-violating parameter and measure the asymmetry $\mathcal{A}$ (see figures 13 - 14) or the regression parity violating observable $\mathcal{P}$ (see figures 16 - 18). Thus, for a measured $\mathcal{A}$ or $\mathcal{P}$, we can extract the parity violating parameter $2T_1T_2/(T_1^2 + T_2^2)$, and hence T_1/T_2, up to statistical accuracies.

Plots of linear trends between the parity violating parameter and the parity violating observables $\mathcal{A}$ and $\mathcal{P}$ look similar. However, the data must be reconstructed from particle tracks. Charged particles, such as $\pi^{\pm}$, are much

more efficiently identified than π^0s. Furthermore, the asymmetry observable $\mathcal{A}$ and the parity-violating observable, $\mathcal{P}$ should be similar for the charged B decay modes as for the neutral B decay modes.

Table 1: Maximal parity-violating values of $\mathcal{A}$ and $\mathcal{P}$ for three neutral B decay modes. Sample sizes are 10,000 events per sample. "σ in $\mathcal{A}$" and "σ in $\mathcal{P}$" are number of standard deviations from $\mathcal{A}$ and $\mathcal{P}$ for maximal parity violation.

decay mode	$\mathcal{A}$	σ in $\mathcal{A}$	$\mathcal{P}$	σ in $\mathcal{P}$
$B \to \gamma K^{\pm}\pi^{\mp}\pi^0$	0.1994 ± 0.0095	20.99	0.20473 ± 0.0091	22.50
$B \to \gamma K^0_S\pi^+\pi^-$	0.1884 ± 0.0098	19.22	0.18465 ± 0.0092	20.07
$B \to \gamma K^0_S\pi^0\pi^0$	0.1906 ± 0.0098	19.45	0.19406 ± 0.0092	21.09

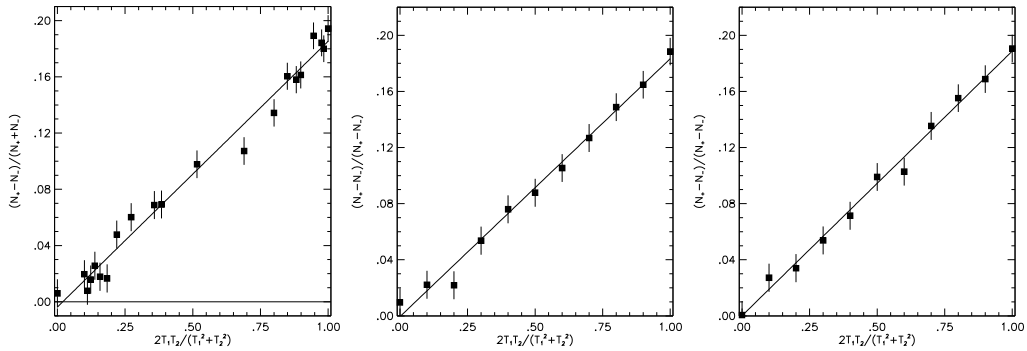

Figure 13: (left) Regression plot using asymmetry observable. For maximal parity violation, $\mathcal{A} = 0.1944 \pm 0.0095$. This is taken for the decay chain $B^0, \overline{B^0} \to \gamma K^{\pm}\pi^{\mp}\pi^0$.

Figure 14: (middle) Regression plot using asymmetry observable. For maximal parity violation, $\mathcal{A} = 0.1884 \pm 0.0098$. This is taken for the decay chain $B^0, \overline{B^0} \to \gamma K^0_S\pi^+\pi^-$.

Figure 15: (right) Regression plot using asymmetry observable. For maximal parity violation, $\mathcal{A} = 0.1906 \pm 0.0098$. This is taken for the decay chain $B^0, \overline{B^0} \to \gamma K^0_S\pi^0\pi^0$.

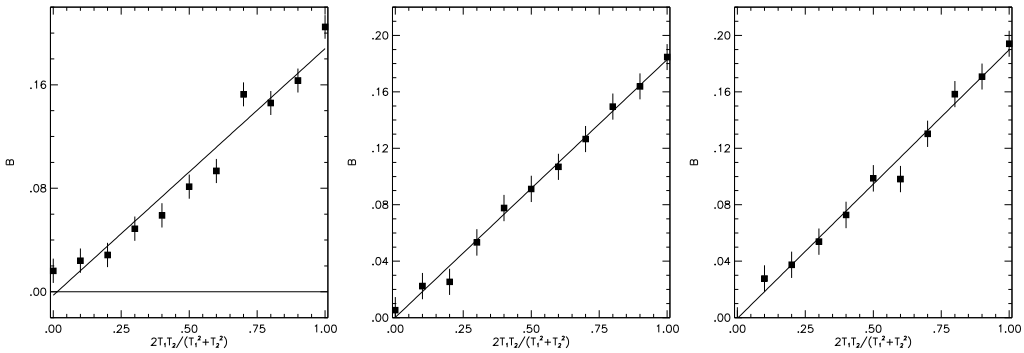

Figure 16: (left) Plot of observable $\mathcal{B}$ vs. parity-violating parameter $2T_1T_2/(T_1^2+T_2^2)$. This is taken for the decay chain $B^0, \overline{B^0} \to \gamma K^{\pm}\pi^{\mp}\pi^0$.

Figure 17: (middle) Plot of observable $\mathcal{B}$ vs. parity-violating parameter $2T_1T_2/(T_1^2+T_2^2)$. For maximal parity violation, $\mathcal{P} = 0.18465 \pm 0.00920$. This is taken for the decay chain $B^0, \overline{B^0} \to \gamma K_S^0\pi^+\pi^-$.

Figure 18: (right) Plot of observable $\mathcal{B}$ vs. parity-violating parameter $2T_1T_2/(T_1^2+T_2^2)$. For maximal parity violation, $\mathcal{P} = 0.1847 \pm 0.0092$. This is taken for the decay chain $B^0, \overline{B^0} \to \gamma K_S^0\pi^0\pi^0$.

7 Reconstruction Background

7.1 Introduction (CLEO Detector and CESR Colliders)

The detection of $B\overline{B}$ meson pairs, which includes an analysis of this decay, occurs at the CESR (Cornell Electron-positron Storage Ring) collider, a B meson factory at Cornell University. The basic schematic diagram of the upgraded detector (i.e. used for CLEO III) is shown in figure 19. The collider is an accelerator that collides electron-positron pairs at a center of mass energy of 10.58 GeV (to create $B\overline{B}$ pairs) and at a center of mass energy of 10.56 GeV (to analyze the behavior of continuum background $q\overline{q}$ pairs). A diagram of the CESR collider is shown in figure 21.

A diagram (see figure 20) of the cross section of e^-e^+ collision depicts the various Υ resonances at a range of collision center-of-mass energies. The $B\overline{B}$ events are produced at the peak of the broad Υ_{4s} resonance for 2/3 of the run time and $q\overline{q}$ continuum events are produced off resonance for 1/3 of the run time of the CESR collider. The beam is run off resonance in order to better understand the continuum backgrounds in $B\overline{B}$ events.

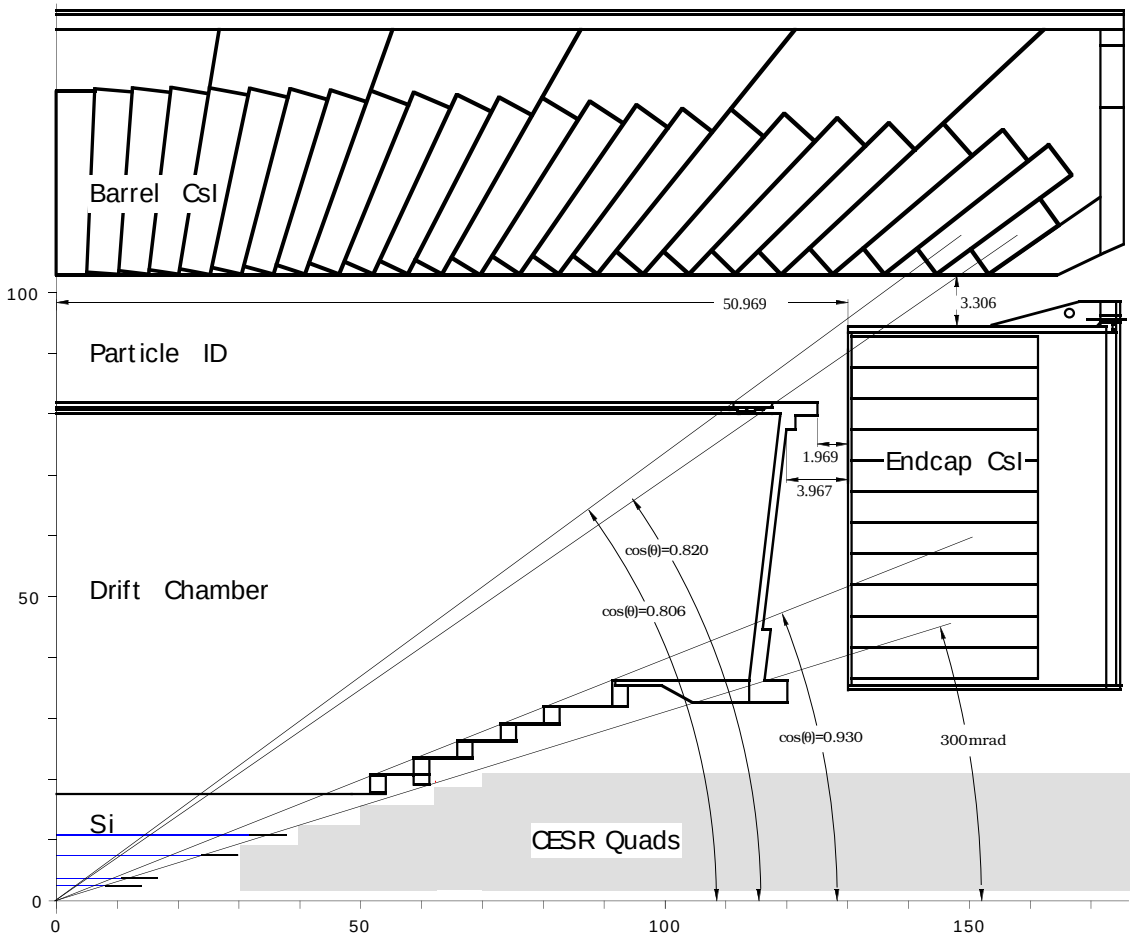

Figure 19: Simplified cartoon of various angular detection "thresholds" for the CLEO detector. The angle is measured from the main axis of the detector. In the data analysis, for example, only showers that lie within the barrels are used, i.e. where $|\cos\theta| < 0.8$.

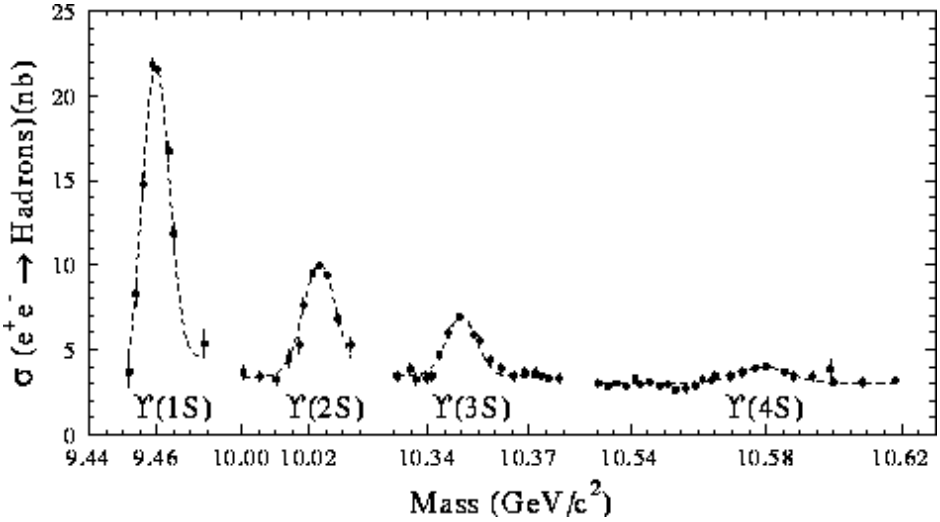

Figure 20: Plot of the various Υ resonances, taken at the CESR collider with the CLEO detector, as a function of center-of-mass energy in e^-e^+ collisions. This analysis focuses on Υ_{4s} resonances, which is especially broad and only barely above background, and produces $B\overline{B}$ pairs. The CESR collider operates 1/3 of the time at $E_{cm} = 10.56$ GeV, to observe $q\overline{q}$ backgrounds, and 2/3 of the time at 10.58 GeV, to observe $B\overline{B}$ backgrounds.

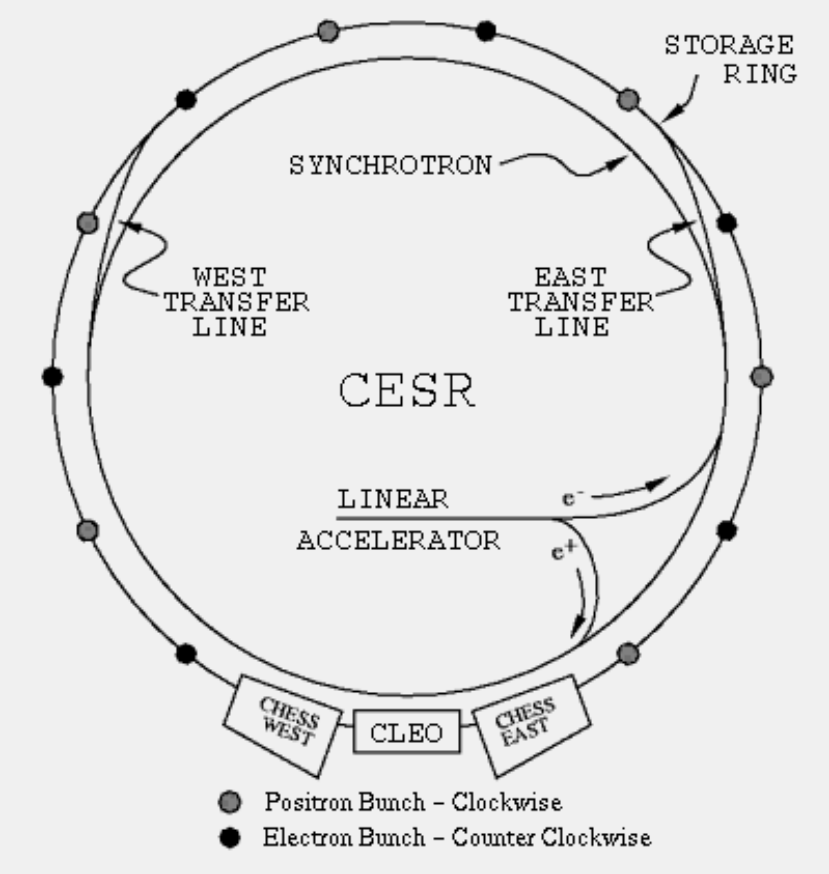

Figure 21: Schematic of the CESR (Cornell Electron-positron Storage Ring), depicting the linear accelerator, storage ring, and CLEO detector.

7.2 Analysis Chain

In general, e^+e^- collisions in the CESR collider produce particles, such as photons and pions, which enter the CLEO detector. The CLEO detector registers events within the drift chamber and the calorimeters. Events within the drift chamber and calorimeter are then reinterpreted as particle showers and tracks, which are then identified as the various decay products due to a collision event.

An analysis of the reconstruction consists of reconstructed data. From data on the showers and tracks simulated in the CLEO detector, to find that particular decay and analyze the data. The diagnostic consists only of determining whether we get the decay $B \to \gamma K \pi\pi$. The analysis chain is shown in figure 22 and consists of the following important steps in the full analysis, which is shown in figure 22:

1. In simulation mode the Monte Carlo event generator simulates events containing the decays of interest. This Monte Carlo simulates particles, such as pions and photons, and events just as those observed in detectors. Another program, CLEOG, simulates the response of the CLEO particle detector. CLEOG simulates raw data such as those seen within the CLEO detector. This raw data consists, in our analysis, pri-

marily of hits within the drift chamber and energy showers within the calorimeter. See figure 19 for a schematic of the CLEO detector.

2. The real data consists of a collision due to the CESR collider within the CLEO detector, and the creation of "hits" within the drift chamber and energy showers within the calorimeter.

3. Both simulated and reconstructed data pass through a second routine, PASS2, which reconstructs both the simulated or real detector "hits" into showers and tracks.

4. The data are organized into ROAR "common blocks," or vectors and matrices, which contain reconstructed particle data used for further analysis. The data are identical for the full Monte Carlo as for the data.

However, due to its complexity, the normal analysis chain consumes many seconds of CPU time through the experimental data and full simulated Monte Carlo. Therefore a much faster detector simulator, TRKSIM, is used; among its disadvantages, however, is the fact that the simulated detector behaves simplistically – that is, detector inefficiencies, resolutions, backgrounds, and pathologies are parametrized.

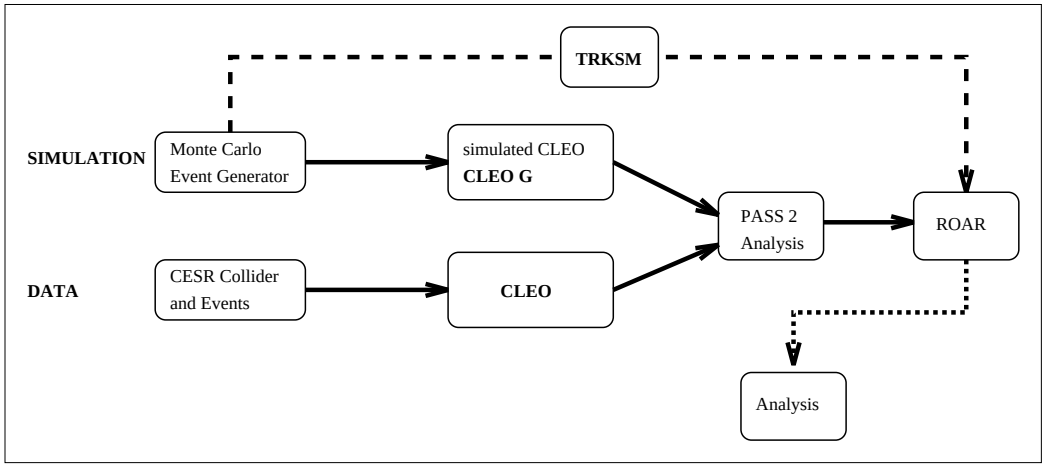

Figure 22: Analysis chain for CLEO data (denoted by **DATA**) and the full CLEO event simulation and detection Monte Carlo (denoted by **SIMULATION**). TRKSIM is shown as a dotted arrow that bypasses the full analyses. Note that TRKSIM bypasses many of these steps and is much faster, although less accurate, than the full analyses.

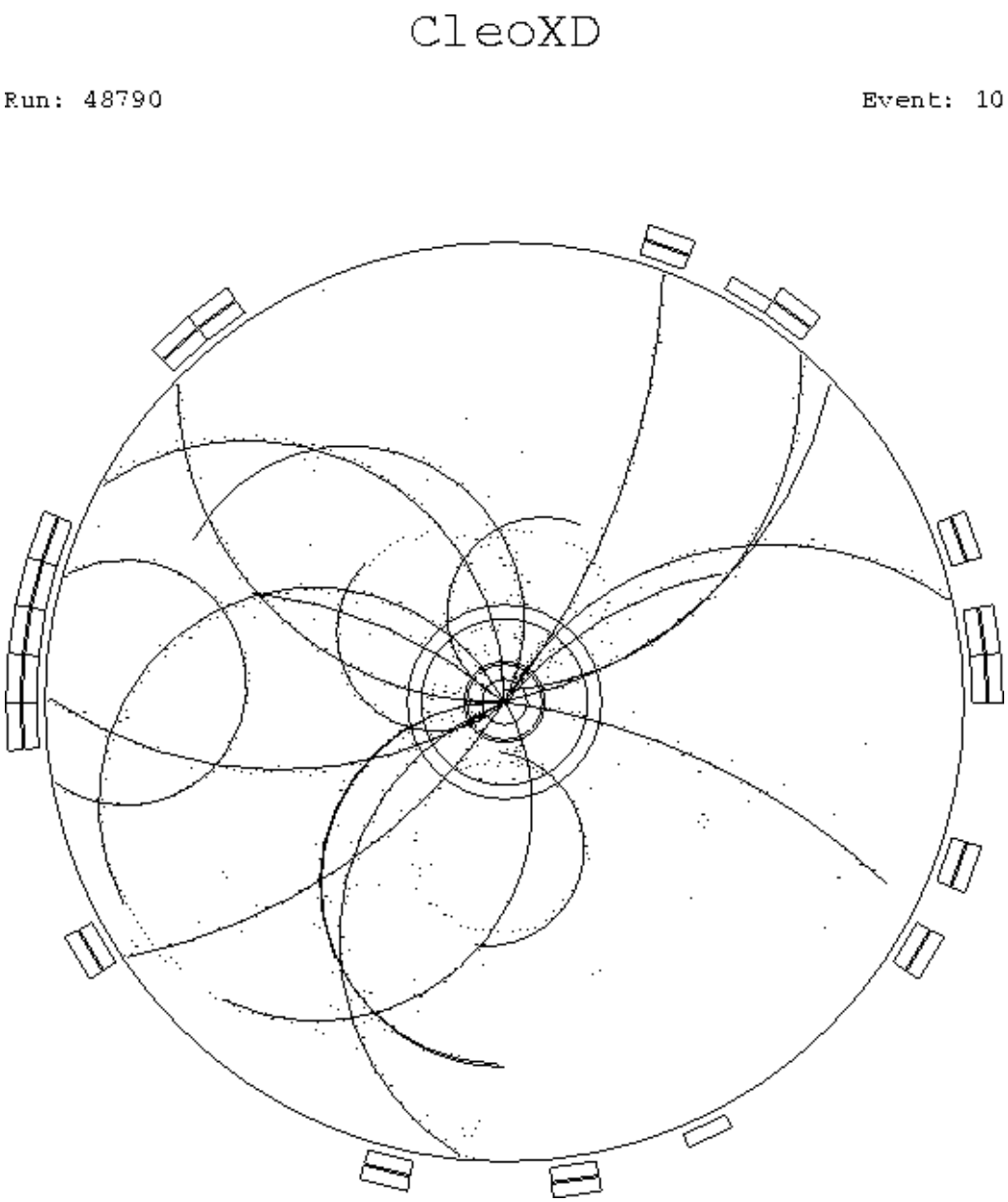

Figure 23: A fully simulated Monte Carlo decay, depicting tracks caused by "hits" within the CLEO drift chamber. Shown here, neutral particles such as photons, as well as charged particles, leave showers in the calorimeter.

8 Cuts

8.1 Introduction, Rationale

Cuts are constraints or criteria that certain sets of data must pass pass in order to be analyzed. For example, a common cut is that *showers* (photons and other neutral particles which deposit energy within the calorimeter) and *tracks* (charged particles which deposit energy within the detector's drift chamber) must lie within a certain angular region of the detector (see figure 19).

There are two general types of cuts on the data: 1) signal selection cuts, which concerns the proper identification of particles and the reconstruction of the decay of interest, and 2) background suppression.

The background consists of isotropic $B\overline{B}$ backgrounds as well as the "jettier" $q\overline{q}$ backgrounds, where q is a light quark.[3] The jettiness arises from the low mass, and hence large momenta, of the light quarks in the continuum background. Furthermore, these continuum background events are $q\overline{q}$ with final state radiation, hence the presence of high energy photons in all continuum background events.

[3] "jetty" events are those in which the decay consistsof two or more jets shooting from a central region – i.e. the momentum distribution is very centralized about two opposite regions.

Note that the $q\overline{q}$ simulation is simulated by the the subroutine "lqq.ctr" with a center-of-mass energy of 10.56 GeV. The signal $b\bar{b}$ signal B production and decay is simulated by the script "bsg.ctr" and further refinements, simulating parity violation in the B meson decay, is simulated through "bsg.dec," at center-of-mass energy 10.58 GeV. Finally, the simulation of a "background" at the signal's center-of-mass energy of 10.58 GeV is performed through the script "bb_4s3.ctr," and $q\overline{q}$ decays are programmed through the script "lqq.ctr."

A cartoon depicting jetty events, corresponding to $q\overline{q}$ backgrounds, and isotropic $B\overline{B}$ signal and backgrounds, are shown in figures 24 - 26.

Event shape variable cuts, such as the Fox-Wolfram moments thrust, sphericity, and other combinations, are relatively good at suppressing "jetty" $q\overline{q}$ backgrounds from the $B\overline{B}$ signals and backgrounds. By far the most important part is background suppression, as continuum backgrounds overwhelm the signal $B \to \gamma K\pi\pi$ decay by 10^5. Furthermore, $\sigma_{q\bar{q}} = 3.1$ nb, while $\sigma_{B\overline{B}} = \sigma_{\Upsilon_{4s}} = 1.07$ nb (see figure 20 for a relative ratio in cross-sections to $B\overline{B}$ and $q\overline{q}$ decays).

Here we discuss signal selection cuts primarily, and then those event shape variable cuts used in the suppression of backgrounds. The signal selection

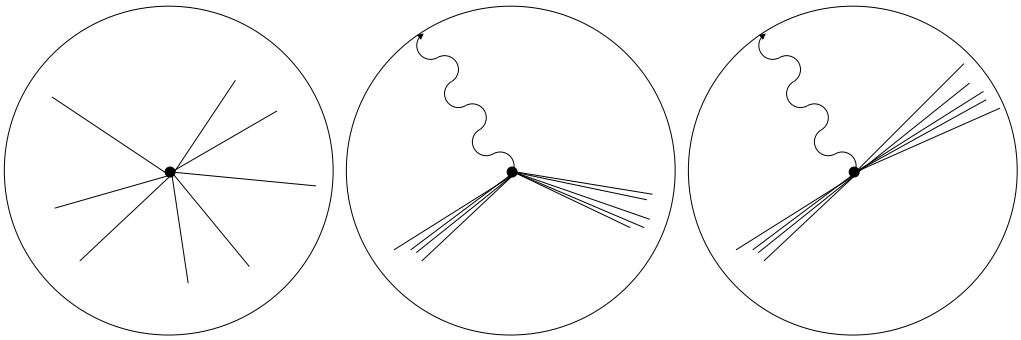

Figure 24: (left) Cartoon of event tracks for a $B\overline{B}$ signal or background event shown here. Note that this event is isotropic. Event shape variable cuts, therefore, should be able to remove a large bulk of $q\overline{q}$ events.

Figure 25: (middle) Cartoon of event tracks for a two-jet $q\overline{q}$ event with a hard photon within here; the recoil consists of all particles except for the photon. Since the momentum and energy of the hard photon dominates the event, there is a significant chance that a jetty event, such as from continuum background, will not be recognized as such.

Figure 26: (right) Cartoon of event tracks for a two-jet event in the photon recoil frame, or proper frame of all particles recoiling from the hard photon. The correct jettiness, with negligible bias from the hard photon, is shown here (i.e. an observable which recorded the event shown in figure 25 as non-jetty would do so here.

cuts consists of proper particle identification, combinatoric reconstruction of

the cut according to invariant mass and total momentum of the combination.

8.2 Particle Identification Cuts

The current reconstruction chain consists of generic particle identification cuts to choose "good" particles for the decay $B^0, \overline{B^0} \to \gamma K^{\pm}\pi^{\mp}\pi^0$. Below we list the "cuts" which the various candidate tracks and showers must pass to be considered "good" photons, $K^{\pm}$'s, $\pi^{\pm}$'s, π^0's, and K^0_S's.

8.2.1 Shower Cuts

Showers deposit their energy into the crystal calorimeter and leave no energy trail (i.e. hits) in the drift chamber (see figure 19). The following *loose* cuts made on the showers, which correspond to relatively low-energy photons. For normal low-energy γ showers, create a bank of stored photon information from the showers. These standard photonic cuts are given below:

1. verify that the shower does not match to charged track, since charged particles also leave showers within the crystal.

2. that the shower lies in the portion of the detector that can reliably measure shower energies well, hence where $|\cos\theta| < 0.95$ (see figure 19 for a schematic).

3. the energy of the shower must be greater than 25 MeV, i.e. the energy

above which the efficiency and energy resolution for showers is well understood.

For high energy γ, the following *tight* cuts are made:

1. Photon energy is greater than 1.8 GeV.

2. Photon is more than 30 cm from the nearest charged track.

3. π^0 *veto*: the high-energy photon cannot correspond to any of the γ used to reconstruct a π^0.

4. lateral energy profile: we must make sure that the lateral energy profile of the shower is consistent with its being a photon to a level of 99% confidence. The measure of the lateral energy profile is the quantity $E9E25$, the ratio of the energy deposited within a 3×3 square crystal to the energy deposited within a 5×5 area; the value $CUT1$ gives a ratio to which one can be certain, to 99% statistical accuracy, that only one high-energy shower has reached this region of the calorimeter.

Shown below, in figures 30 and 31 are relative energy profiles seen for "good" and "bad" showers over a 5×5 square of crystal calorimeters.

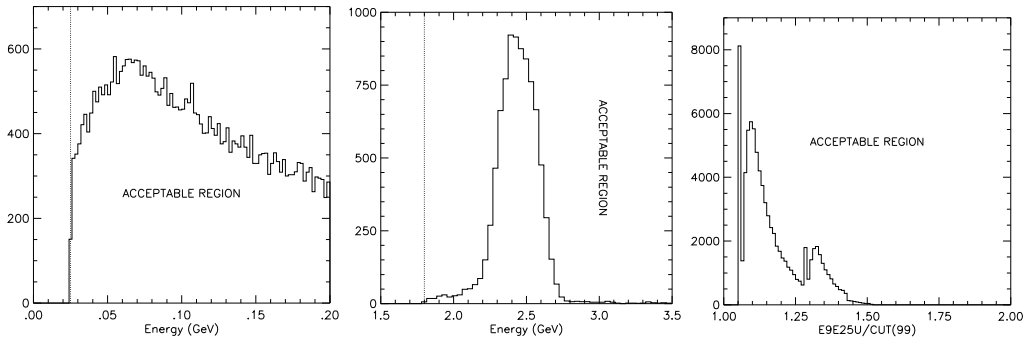

Figure 27: (left) Energies of candidate photons (i.e. showers) used in π^0 reconstruction. We use showers whose energies are greater than 25 MeV.

Figure 28: (middle) Energies of high-energy photons whose energy is greater than 1.8 GeV. These are photons used in the reconstruction of the B meson decay.

Figure 29: (right) Statistical measure of the lateral energy profile of neutral showers, $E9E25/CUT1$, where $E9E25$ is the ratio of the shower energy deposited within the central three-square crystal to the energy deposited within the rest of a five-square crystal. $CUT1$ is a value for $E9E25$, for a given shower energy, that is statistically significant at the 0.99 level. Acceptable high energy photons are those in which the lateral energy shower profile quantity is greater than 1. Since TRKSIM simulates the detector, this quantity is always greater than 1.0.

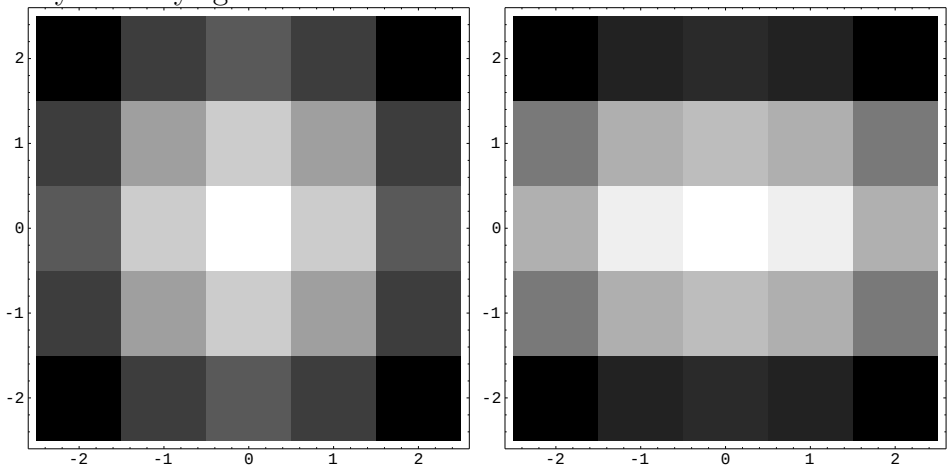

Figure 30: (left) Relative energy profile for a good shower, in which nearly all the energy is deposited within a central 3×3 square array detectors.

Figure 31: (right) Relative energy profile for a bad shower, in which we have two shower hits centered at detectors (-2,0) and (2,0). As shown, there is no symmetric energy profile for this two-shower hit.

8.2.2 Track Cuts

For the given decay in consideration, the following cuts are associated with charged tracks.

1. Each charged track has an associated shower.

2. The charged tracks must lie within the region of the detector in which the momentum and energy resolution of these charged tracks is reasonably high, hence where $|\cos\theta| < 0.8$, where θ is the angle between the long axis of the beam pipe and the three-momentum of the charged track.

3. The average deviation of detector "hits," as seen by anode wires within the drift chamber, about the "best-fit" path, or $RESICD$, must be less than 0.5 mm.

4. Associated with each charged track are quantities $SGKADI$ and $SGPIDI$, associated with how "well" this track corresponds to a charged kaon or pion, respectively. The only manner in which to distinguish charged kaons and pions is through their ionization profile, dE/dx, measured in the drift chamber by anode wires; to a limiting energy, both charged pions and kaons deposit energy in the drift chamber in a characteristic

manner, as illustrated in figure 35. $SGKADI$ and $SGPIDI$ represent the standard deviation of the average energy deposited per sample to the expected energy deposited per sample by kaons and pions, respectively. See figures 32 and 33 for the distributions of $SGKADI$ and $SGPIDI$.

5. In reconstructing $B^0, \overline{B^0} \to \gamma K^{\pm}\pi^{\mp}\pi^0$ decays, a charged track will be considered a pion if $|SGPIDI| < 3$ and will be considered a charged kaon if $|SGKADI| < 3$.

6. Furthermore, if a particle has been chosen to be a "good" combination, then the mass of the charged track is changed to 0.49767 GeV, the mass of the $K^{\pm}$, and its energy is scaled accordingly.

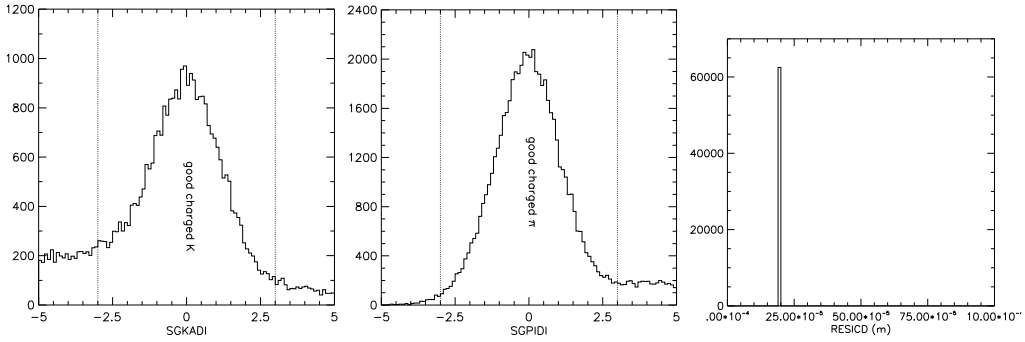

Figure 32: (left) $SGKADI$, a measure of, for a given charged kaon momentum, how many standard deviations away is the ionization within the drift chamber away from the predicted ionization a $K^{\pm}$ deposits within the drift chamber. "Good" $K^{\pm}$ are those where $|SGKADI| < 3$. The tail at high values of $SGKADI$ correspond to $\pi^{\pm}$.

Figure 33: (middle) $SGPIDI$, a measure of, for a given charged pion momentum, how many standard deviations away is the ionization from the predicted amount of ionization a $\pi^{\pm}$ deposits within the drift chamber. "Good" $\pi^{\pm}$ are those where $|SGPIDI| < 3$. The tail at low values of $SGPIDI$ correspond to $K^{\pm}$.

Figure 34: (right) charged particles follow curved paths within a magnetic field. Hits within the drift chamber are centered about the path of the particle, typically ten to twenty hits per particle. The average deviation of these hits from the "best-fit" estimate of the path of the charged track is $RESICD$. This figure depicts $RESICD$ for all tracks. Good tracks are those in which $RESICD < 0.005$ m. Note that since we are employing TRKSIM to simulate the behavior of the detector, that $RESICD$ is always at a given value.

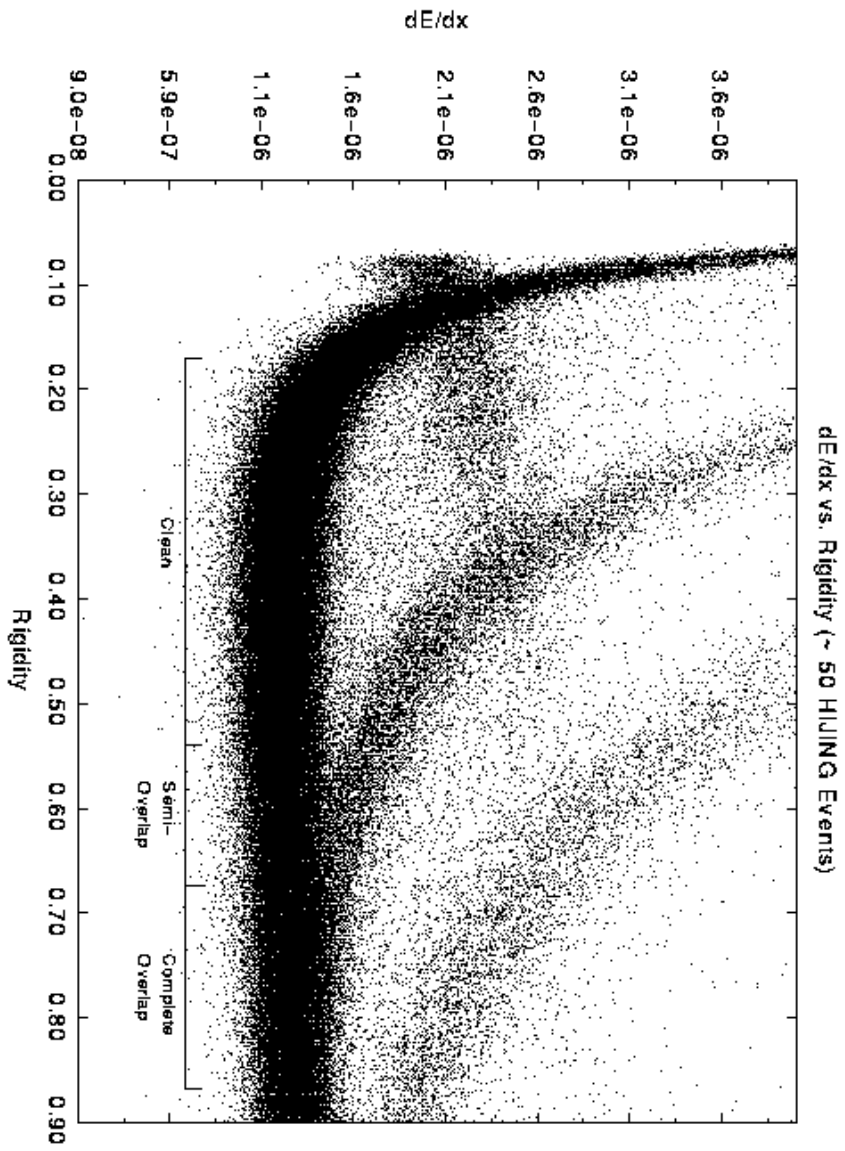

Figure 35: Plot of dE/dx as a function of particle rigidity; the lowest branch corresponds to $\pi^{\pm}$, the next highest correspond to $K^{\pm}$, and the highest branch to protons. The faint convex branch corresponds to $e^{\pm}$. Note that beyond a rigidity of 0.8, it becomes impossible to distinguish, based on ionization characteristic, charged pions and kaons.

8.2.3 π^0 Cuts

In constructing a π^0 bank, we employ the following sets of cuts; associated with these cuts are thorough explanations of what is being done.

1. Each photon from a π^0 decay must lie within the portion of the detector that accurately measure lower energy photons, hence where $|\cos\theta| < 0.8$.

2. A statistical measure of the difference in invariant mass of the two-photon system, given by the following:

$$S_{\gamma\gamma} = \frac{m_{\gamma\gamma} - m_{\pi 0}}{\sigma_{\gamma\gamma}} \tag{39}$$

   where $m_{\gamma\gamma}$ is the mass of the 2-photon system, $m_{\pi 0} = 0.135$ GeV is the mass of the π^0, and $\sigma_{\gamma\gamma}$ is the expected uncertainty in the two-photon mass. The value of this quantity must be less than 3.0, i.e. $|S_{\gamma\gamma}| < 3.0$.

3. None of the photons which constitute this can correspond to the high-energy photon; neither photon must correspond to each other.

Plots of those π^0 from all events in a simulation are shown in figures 36 and 37 and plots from events in which at least one B combination passed the cuts

are shown in figures 38 and 39).

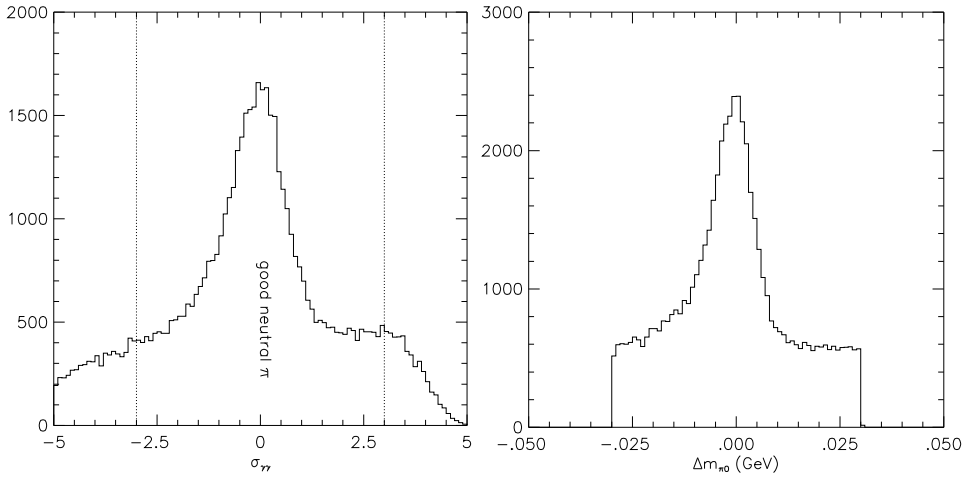

Figure 36: (left) Distribution of $S_{\gamma\gamma}$. We consider a pion to be "good" only when the mass is within 3 standard deviations of the true π^0 mass, 0.135 GeV. Note, here, the large combinatoric background beneath the peak.

Figure 37: (right) Distribution of the invariant mass of the two-photon system about the true π^0 mass of 0.135 GeV. Note the *large* flat combinatoric background corresponding to misreconstructed π^0, above which the peak sits.

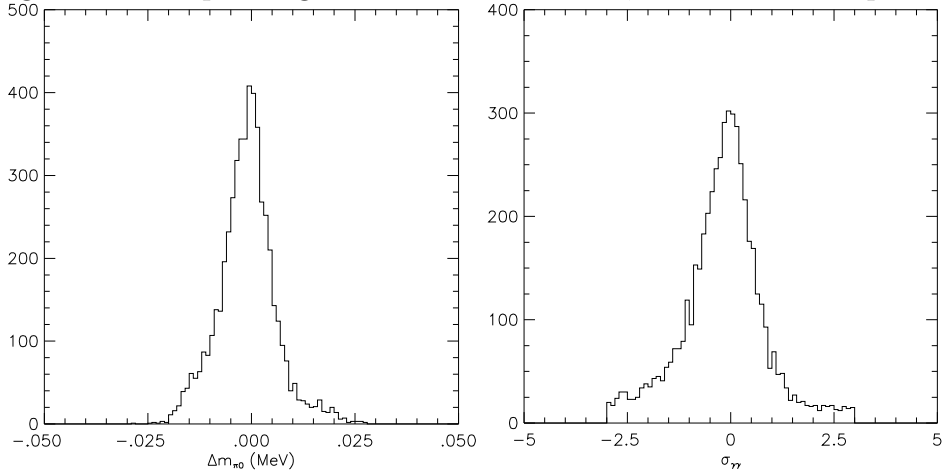

Figure 38: (left) Plot of the reconstructed π^0 mass for those "true" B decay events. Note the lack of a combinatoric background.

Figure 39: (right) Plot of the parameter $\sigma_{\gamma\gamma}$ for those "true" decay modes. Note the lack of a combinatoric background.

8.2.4 K_S^0 Cuts

In constructing a K_S^0 bank, we employ the following sets of cuts; associated with these cuts are thorough explanations of what is being done. Here we make the following cuts on being a good K_S^0:

1. The charged pions which make up these K_S^0 are themselves good charged tracks, thus that $|\cos\theta| < 0.8$.

2. The associated χ^2 value for the fit of two charged tracks to form a K_S^0 must be less than 3. This χ^2 value is formed by determining the deviation of charged tracks about their path, as well as (and for TRKSIM, primarily by this method) how well these two charged tracks "fit" to form a K_S^0.

3. The distance that the reconstructed momentum of the K_S^0 "misses" the center of the beam, or $RBMTX$, must be less than 0.5 mm.

4. The reconstructed mass of the K_S^0 must be less than 0.015 GeV from the true mass of the K_S^0, 0.49767 GeV.

Plots detailing the above variables are shown in figures 40, 41, and 42.

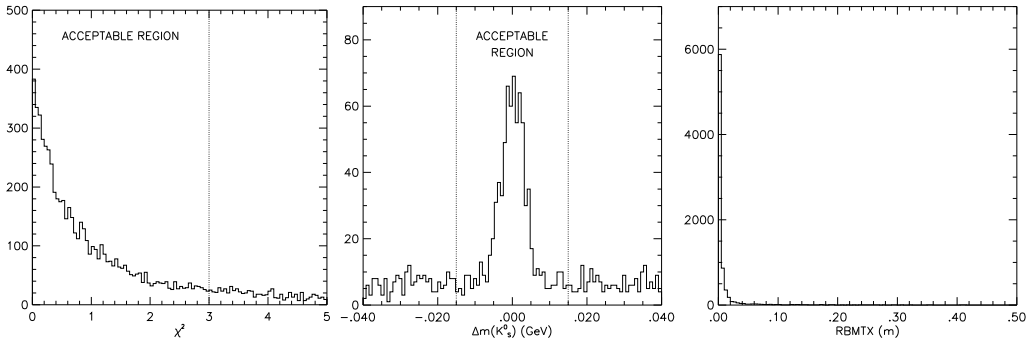

Figure 40: (left) Distribution of χ^2 for K_S^0 candidates. We choose only those K_S^0 whose $\chi^2 \leq 3$.

Figure 41: (right) Distribution of deviation of reconstructed K_S^0 mass from true mass of 0.498 GeV. We require that for a candidate, $\left|\Delta m_{K_S^0}\right| \leq 0.015 GeV$.

Figure 42: (left) The distance that the reconstructed K_S^0 spatial momentum "misses" the central axis of the detector. TRKSIM does not, here, include the background, for which the deviation is more severe.

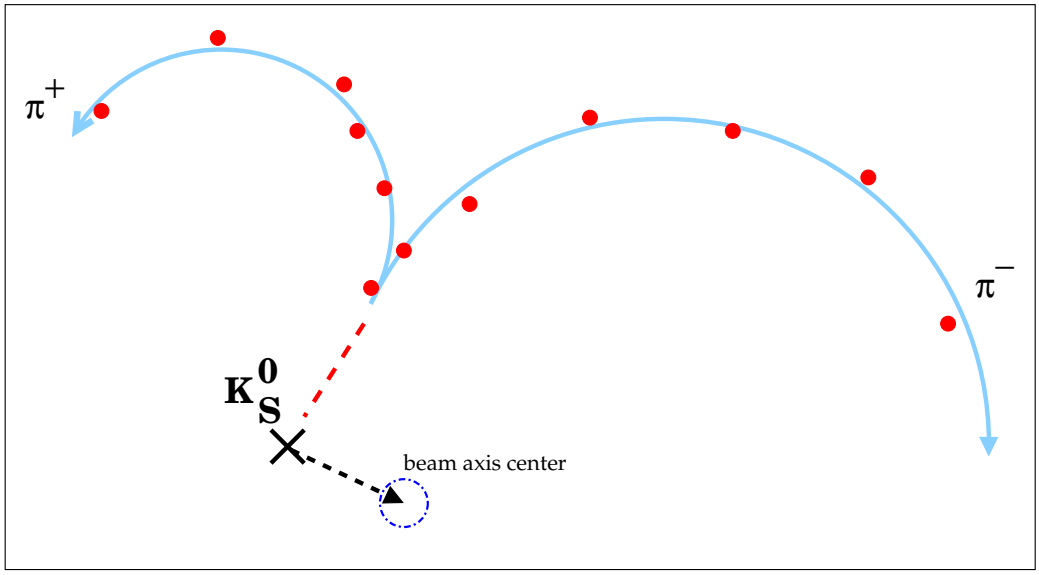

Figure 43: (right) A schematic cartoon explaining, in rough terms, the basic elements of a K_S^0 reconstruction. Two charged pions are reconstructed and their best-fit paths are determined; if these tracks meet, then they are fitted into a best-estimate reconstructed K_S^0 – note that dots along the paths denote "hits" within the drift chamber. Also from these is the quantity $RBMTX$, the minimum approach distance of the reconstructed K_S^0 momentum to the beam axis.

8.3 Combinatoric Cuts

The overall decay in question is $B \rightarrow \gamma K \pi\pi$. This occurrs via six possible decay modes: 1) $B^0, \overline{B^0} \rightarrow \gamma K^{\pm}\pi^{\mp}\pi^0$, 2) $B^0, \overline{B^0} \rightarrow \gamma K^0_S \pi^+\pi^-$, 3) $B^0, \overline{B^0} \rightarrow \gamma K^0_S \pi^0\pi^0$, 4) $B^{\pm} \rightarrow \gamma K^{\pm}\pi^{\mp}\pi^{\pm}$, 5) $B^{\pm} \rightarrow K^{\pm}\pi^0\pi^0$, and 6) $B^{\pm} \rightarrow \gamma K^0_S \pi^{\pm}\pi^0$. We implement a "combinatoric machine" that searches through all six modes in the following manner. However, although during the preliminary reconstruction, we analyzed only the three neutral B decay modes, during the progress of this project, we have analyzed the highest-efficiency mode – $B^0, \overline{B^0} \rightarrow \gamma K^{\pm}\pi^{\mp}\pi^0$.

1. $B^0, \overline{B^0} \rightarrow \gamma K^{\pm}\pi^{\mp}\pi^0$: first loop through the high-energy photons. Second, loop through the charged tracks to look for $K^{\pm}$ candidates. Third, loop through charged tracks to look for $\pi^{\pm}$ candidates of opposite sign of the kaon; make sure that the pion is not the same track as the kaon. Finally, loop through the π^0 candidates, making sure that none of the π^0 photons correspond to the high-energy photon. Change the mass of the kaon candidate to the charged kaon mass, and change its energy to correspond to that of a charged kaon.

2. $B^0, \overline{B^0} \rightarrow \gamma K^0_S \pi^+\pi^-$: first loop through the high-energy photons. Sec-

ond, loop through the K_S^0 candidates. Third, loop through the charged tracks looking for a π^+, such that the charged track does not correspond to the K_S^0 descendants. Fourth, loop through the charged tracks looking for a π^-, such that the charged track does not correspond to the K_S^0 charged pions.

3. $B^0, \overline{B^0} \to \gamma K_S^0 \pi^0 \pi^0$: first, loop through the high-energy photons. Second, loop through the K_S^0 candidates. Third, loop through the π^0 candidates, making sure none of its descendants correspond to the high-energy photon. Fourth, loop through the π^0 candidates, making sure that none of its descendants correspond to either the high-energy photon or to the descendants of the other π^0.

4. $B^\pm \to \gamma K^\pm \pi^\mp \pi^\pm$: First, loop through the high-energy photons. Second, loop through the charged tracks looking for $K^\pm$ candidates. Third, loop through charged tracks looking for $\pi^\pm$ candidates of the opposite sign of the kaon, making sure that the pion does not correspond to the kaon. Fourth, loop through the charged tracks looking for $\pi^\pm$ candidates of the same sign of the kaon, making sure that the pion does not correspond to the kaon. Change the mass of the kaon candidate to the

charged kaon mass, and change its energy to correspond to that of a charged kaon.

5. $B^{\pm} \to \gamma K^{\pm}\pi^0\pi^0$: First, loop through the high-energy photons. Second, loop through the charged tracks looking for a $K^{\pm}$ candidate. Third, loop through the π^0 candidates, making sure that none of its descendants correspond to the high-energy photon. Fourth, loop through the π^0 candidats, making sure that none of its descendants correspond either to the high-energy photon or the descendants of the other π^0. Change the mass of the kaon candidate to the charged kaon mass, and change its energy to correspond to that of a charged kaon.

6. $B^{\pm} \to \gamma K^0_S\pi^{\pm}\pi^0$: First, loop through the high-energy photons. Second, loop through the charged tracks looking for a K^0_S candidate. Third, loop through the charged track candidates looking for a $\pi^{\pm}$, checking that it does not correspond to the descendants of the K^0_S. Fourth, loop through the π^0 candidates, making sure that none of its descendants correspond to the high-energy photon.

In this analysis, we focus on only $B^0, \overline{B^0} \to \gamma K^{\pm}\pi^{\mp}\pi^0$ decays. Furthermore, we choose *only* that combination which results in the best B meson. This is

the $\gamma K\pi\pi$ combination closest in mass to $m_B = 5.28$ GeV. Although we may be artificially biasing the distribution for background ($B\overline{B}$ and $q\overline{q}$ events) with this choice, however their frequencies are small enough that we may ignore their effects (after making the appropriate cuts). Plots of the cosine helicity angle distribution for the decay $B^0, \overline{B^0} \to \gamma K^{\pm}\pi^{\mp}\pi^0$, are shown in figures 44 and 45.

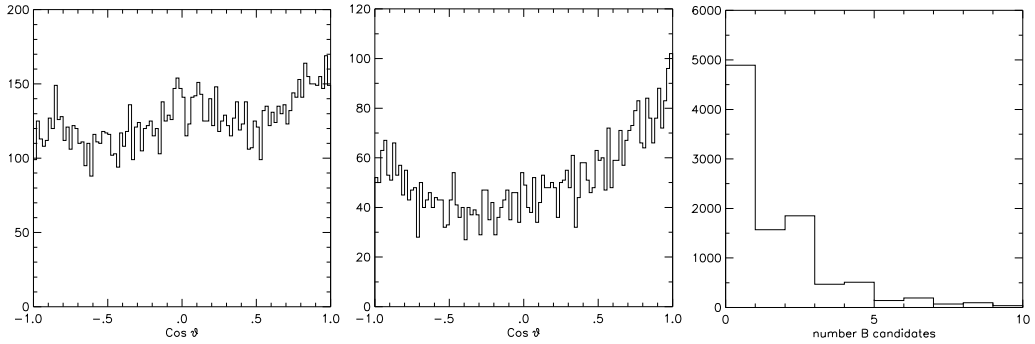

Figure 44: (left) Here is the cosine of the K_1 helicity angle for the case where we have included all candidate B mesons which pass the cut. Note that there is no picture of the normal helicity angle distribution.

Figure 45: (middle) Distribution of the cosine of the K_1 helicity angle for that case in which we have chosen the "best" combination B meson. As expected, no parity violation.

Figure 46: (right) Number distribution of candidates (i.e. all combinations which have passed the cuts.

8.4 Selection of Signal and Sideband Regions

The only criteria associated with choosing an appropriate combination are the total kinematic variables: ΔE, the difference between the sum of the energies of the candidate particles and half the beam energy $E_{beam} = E_{cm}/2 =$ 5.29 GeV; and the beam energy constrained mass, $M_{beam} = \sqrt{E_{beam}^2 - |\mathbf{p}|^2}$, where $\mathbf{p}$ is the total 3-momentum of the system of $\gamma K\pi\pi$. We use these variables because $E = E_{beam} = 5.29$ GeV and $M_{\gamma K\pi\pi} = M_B = 5.29$ GeV are strongly correlated, since both depend on the energy of the $\gamma K\pi\pi$ system. However, ΔE and M_{beam} are largely uncorrelated, and the resolution in M_{beam} is approximately 3 MeV, whereas the resolution in $M_{\gamma K\pi\pi}$ is of the order of 50 MeV; the independence of these two variables allows us to subtract out more of the background without sacrificing signal.

It was determined that a large majority of misreconstructions are due mainly to employing the "wrong" candidate π^0, and a secondary amount due to switching around the charged kaon and the charged pion – this is due to the fact that the only determination of identity for the charged pion and kaon is dE/dx – at energies above 500 MeV, it is no longer possible to distinguish the two candidates apart (see figure 35). The misreconstructions due to using the "wrong" π^0 is due to the fact that there a relatively *large*

number of low-energy ($E < 100$ MeV) photons (see figure 27).

A diagram of various regions of the two-dimensional plot of M_{beam} versus ΔE is shown in figure 47; a density plot in these two dimensions, i.e. figure 48, depicts the signal decay peak. Furthermore, we make plots of the

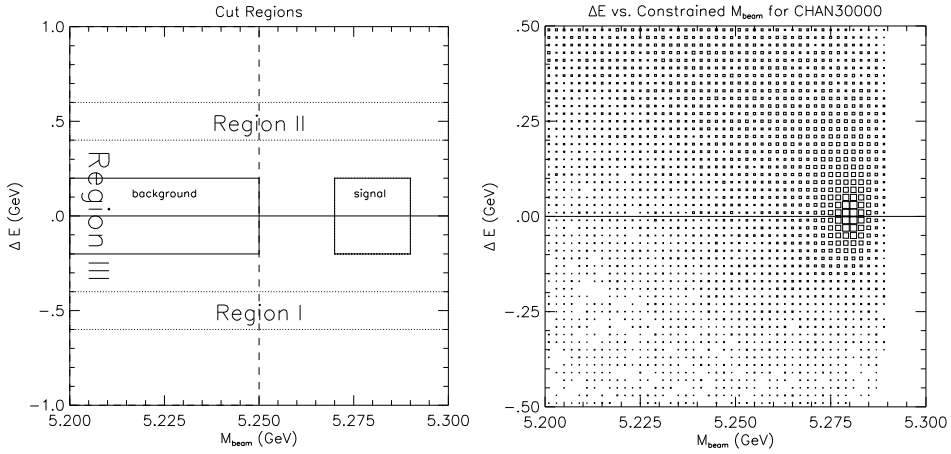

Figure 47: (left) Different plotting areas of M_{beam} vs. ΔE plot. Plots of M_{beam} are made in "signal" and "background" regions (see figure 52). "Region I" corresponds to a plot of M_{beam} (see figure 49), and likewise "Region II" (see figure 50). Finally, "Region III" corresponds to plot of ΔE (see figure 51).

Figure 48: (right) ΔE vs. M_{beam} for decay chain $B^0, \overline{B^0} \to \gamma K^{\pm}\pi^{\mp}\pi^0$. Note the peak at the B mass; that is, the region in which M_{beam} (on vertical axis) is centered about 5.28 GeV and ΔE (on horizontal axis) is centered about 0 GeV.

various regions within the "grand sideband," namely in regions I, II, and III shown in figure 47. These plots are shown in figures 49 - 51. Here, we note that the peak is superimposed above a misreconstruction background. This

misreconstruction background is depicted in figure 50; although technically not due to the continuum background, we find that an ARGUS fit function represents this misreconstruction background well. The ARGUS fit function is the following:

$$N(x) = P_1 x \sqrt{1 - \left(\frac{x}{M_B}\right)^2} \exp\left\{P_4 \left[1 - \left(\frac{x}{M_B}\right)^2\right]\right\} \tag{40}$$

In order to determine a "good" $\gamma K\pi\pi$ combination, we require that ΔE, the difference in the beam energy of the CLEO detector (5.290 GeV) and the sum of the energies of the daughter particles, be between -0.2 GeV and 0.2 GeV (see figure 53). We also require the beam energy constrained mass M_{beam} lie between 5.27 GeV and 5.29 GeV (see figure 52).

In addition, we store combinations within the sideband region, or those $\gamma K\pi\pi$ combinations for which -0.2 GeV $< \Delta E <$ 0.2 GeV and $5.20 GeV < M_{beam} < 5.25 GeV$ (see figures 52 and 48). In this Monte Carlo simulation of the signal B decay, the sidebands correspond to misreconstructions (i.e. one or more bad kaons or pions) of the candidate.

We use the ARGUS fit function on the signal and sideband regions to determine the ratio of misreconstructed background in the signal region to

the sideband region. *Sideband-subtracted* plots of the cosine helicity angle are constructed by subtracting the sideband cosine helicity angle distribution, with the proper correcting factor, from the signal region cosine helicity angles (see figure 54).

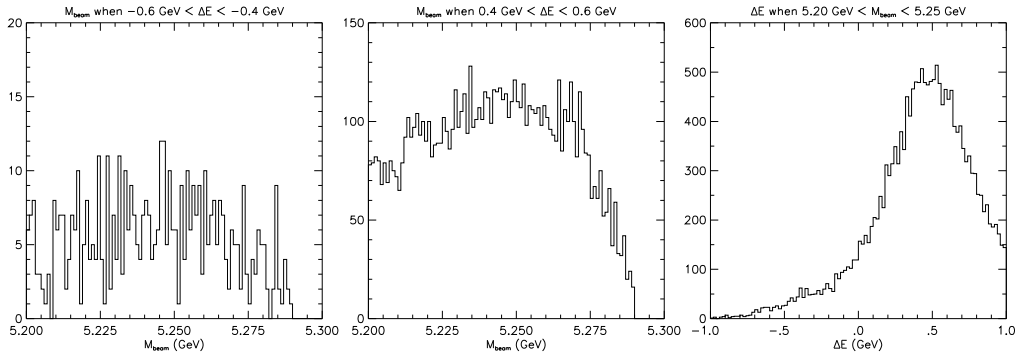

Figure 49: (left) Plot of M_{beam} where -0.6 GeV $< \Delta E <$ -0.4 GeV, which corresponds to Region I in figure 47. Note the paucity of points.

Figure 50: (middle) Plot of M_{beam} where 0.4 GeV $< \Delta E <$ 0.6 GeV. M_{beam} is centered about $5.25 GeV$. Note that this corresponds to the shape of the background function shown in figure 52. This region corresponds to Region II shown in figure 47.

Figure 51: (right) Plot of ΔE where 5.20 GeV $< M_{beam} <$ 5.25 GeV. This corresponds to Region III in figure 47. Note the marked asymmetry in this distribution of ΔE.

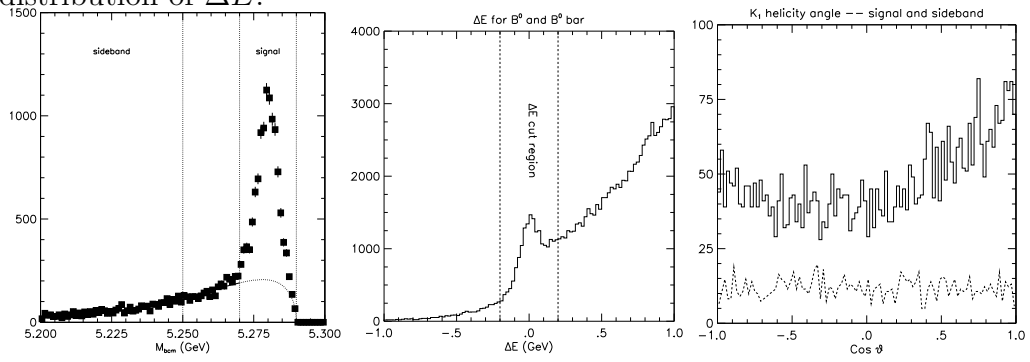

Figure 52: (left) Regions of interest in the histogram plot of constrained M_{beam} for combinations in which -0.2 GeV $< \Delta E <$ 0.2 GeV. The signal data comes from the peak (5.27 GeV $< M_{beam} <$ 5.29 GeV); the sideband which is to be subtracted is collected from region where 5.20 GeV $< M_{beam} <$ 5.25 GeV. In addition, the ARGUS background function is superimposed on the distribution to give a clearer representation of the relative weights of the background in the signal and background regions.

Figure 53: (middle) Raw plot of ΔE. Note the presence of a large background outside the "cut" region, as well as the noticeable peak in the region of interest.

Figure 54: (right) Plot of raw K_1 cosine helicity angle distribution (in solid) in signal, superimposed with properly scaled K_1 background helicity angle distribution from sideband. Taken from maximum parity violation case.

8.5 Event Shape Variable Cuts

Quantities which are effective at suppressing "jetty" events are the second Fox-Wolfram moments, the sphericity, and thrust (as described below). All three quantities, and other event-shape variables; these extra variables include the cosine of the angle between the "hard" (high-energy) photon and the thrust of the recoil, cosine of the angles between the thrusts of the two B mesons, and the cosine of the thrust of the other B (i.e. not signal B^0) and the hard photon. Here, we find that the cosine of the thrust between the two B mesons is isotropic for signal events, while being definitely nn-isotropic for background $q\overline{q}$ and $B\overline{B}$ events.

The Fox-Wolfram moments are given by the following equations [11]:

$$H_k = \sum_{ij} |\mathbf{p}_i|\,|\mathbf{p}_j|\,P_k\left(\cos\theta_{ij}\right) \tag{41}$$

$$R_k = \frac{H_k}{E_{cm}} \tag{42}$$

Where E_{vis} is the visible energy of the event, $|\mathbf{p}_i|$ is the magnitude of the spatial momentum of particle i, and θ_{ij} is the angle between hadrons i and j. P_k is the k^{th} order normalized Legendre polynomial. R_0 is a measure of energy conservation, so if we ideally measure all the energy (10.56 GeV)

within an event, then $R_0 = 1$. Furthermore, R_1 is a measure of momentum conservation. Ideally, we would have that $R_1 = 0$ in the two systems in which we measure this quantity: the $\gamma K\pi\pi$ system in the lab frame, and the photon recoil system $K\pi\pi$ in its own rest frame. Finally, for jetty events we have that $R_2 = R_0$ for perfectly jetty events, while for spherical events $R_2 = 0$. In both cases, we expect spherical events, so that $R_2 \to 0$.

The sphericity S of an event is given by the following:

$$S = \frac{3}{2}\min\left(\frac{\sum_a p^a_{norm} \cdot\ pa_{norm}}{\sum_a p^a \cdot p^a}\right) \tag{43}$$

$$S = \frac{3}{2}\left(\lambda_2 + \lambda_3\right) \tag{44}$$

Where p^a_{norm} is the 3-momentum vector of particle a which is transverse to some axis that minimizes S, and λ_2 and λ_3 are the second and third eigenvalues, respectively, of the momentum tensor formed by an aggregation of particles. For jetty events $S \to 0$ while for isotropic events $S \to 1$.

The thrust T of an event is found in the following way:

$$T = \max\left(\frac{\sum_a p^a \cdot e_T}{\sum_a p^a}\right) \tag{45}$$

where e_T is the thrust axis of the event. Jetty events have thrusts approaching 1, while isotropic events have thrust approaching zero; thrusts are always negative. Finally, we have also made plots of the cosine of the photon with the thrust axis, $\cos\theta_{thrust}$, for the $K\pi\pi$ system in the photon recoil frame (i.e. $K\pi\pi$ rest frame) and the lab frame. As shown in figures 25 and 26, an obviously jetty event will not be noticed automatically as an especially "jetty" event in the lab frame, but will be notice in the photon recoil frame.

Furthermore, we define additional event shape variables, such as the the cosine of the angle between the thrusts axes of both B mesons (i.e. the candidate B and the other B), as well as the cosine of the thrust axes between the "hard" photon and either the candidate B or the other B. These procedures are useful in eliminating $q\overline{q}$ continuum backgrounds as well as $B\overline{B}$ resonance backgrounds – as shown, these events are much "jettier" than signal $B^0, \overline{B^0} \to \gamma K^{\pm}\pi^{\mp}\pi^0$ decays.

Here I analyze the measures of event shape variables R_2, S, T, and $\cos\theta_{TT}$, the cosine of the angle between the two thrust axes of the two B mesons. Second, the 4-momentum of the photon recoil is defined as $p_{beam} - p_{\gamma}$, where:

$$p_{beam} = (0, 0, 0, E_{beam}) \tag{46}$$

Thus, we can take into account that energy may be lost in the form of neutrinos or other particles which are not recorded by the detector. Event shape variables are chosen to most efficiently suppress the background, and so increase the signal to background ratio.

Below, shown in figures 55 and 56 are plots of the angle between the thrust axis of the $\gamma K\pi\pi$ system and the thrust axis of the other particles in this system, or the cosine of the thrust axes between the two B mesons – $\cos\theta_{TT}$. Plots are taken in both the lab frame and the rest frame of the recoiling B. Note the increased "jettiness" of background events, about which we can very efficiently suppress backgrounds.

To combat overwhelming levels of continuum background, we make the following cuts on the event shape variables are the following. These cuts, although removing 2/3 of the signal decay, remove relatively much more of the background.

1. R_2, the second Fox-Wolfram moment, for the event in the lab frame must be less than or equal to 0.5.

2. T, the thrust of the event in the photon recoil frame, must be smaller than 0.7.

3. $\cos\theta$, where θ is the angle between the thrust axis of the $\gamma K\pi\pi$ system and the rest of the particles in the lab frame, must be between -0.4 and 0.4.

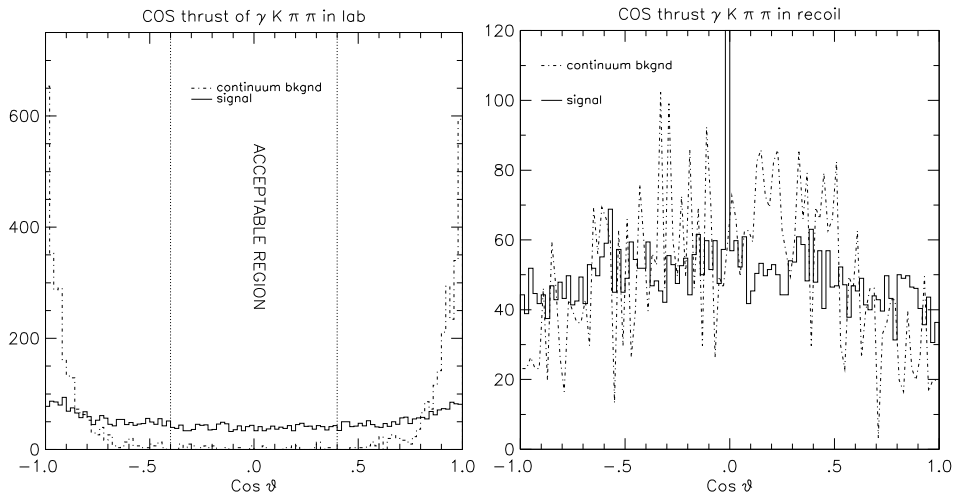

Figure 55: (left) Plot of the cosine of the angle between the $\gamma K\pi\pi$ thrust axis and the thrust axis of the rest of the particles, in the lab frame. Note the parabolic distribution of $\cos\theta_{TT}$. The continuum is dented by a line-dotted histogram, while the signal distribution is denoted by a solid histogram. A cut here is made, $|\cos\theta_{TT}| < 0.40$, where θ_{TT} is the angle between the two reconstructed B mesons

Figure 56: (right) Plot of the cosine of the angle between the $\gamma K\pi\pi$ thrust axis (candidate B) and the thrust axis of the rest of the particles (i.e. other B), in the rest frame of the other B..

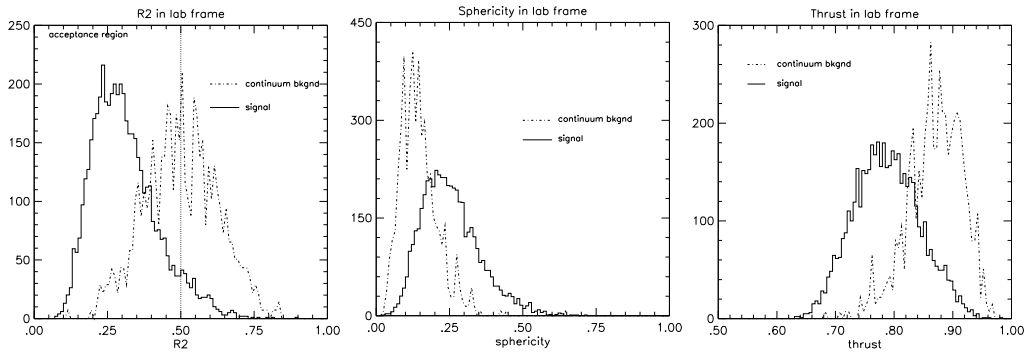

Figure 57: (left) Normalized plots (to area = 5000) of the comparison between the signal simulation, highest mode (for 10000 events) and the "scaled" background simulation (for 100,000 events, scaled as described below). Here, the cut shown is that we allow *only* those events in which $R_2 \leq 0.5$. These are quantities taken in the lab frame.

Figure 58: (middle) Normalized comparative plots (to area = 5000) of the signal simulation simulation and the scaled background simulation. These are taken in the lab frame.

Figure 59: (right) Normalized comparative plots (to area = 5000) of the signal MC simulation and "scaled" background simulation of the thrust magnitude. These are taken in the lab reference frame.

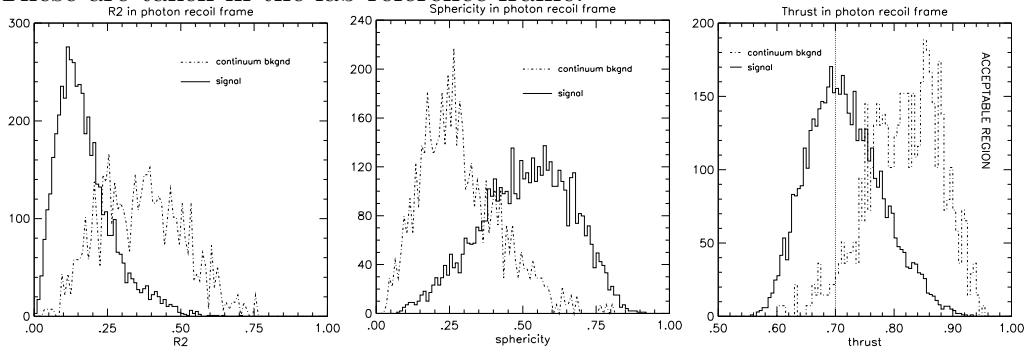

Figure 60: (left) Normalized plots (to area = 5000) of the comparison between the signal simulation, highest mode (for 10000 events) and the "scaled" background simulation (for 100,000 events, scaled as described below). These data were taken in the photon recoil frame.

Figure 61: (middle) Normalized comparative plots (to area = 5000) of the signal simulation simulation and the scaled background simulation. These are taken in the photon recoil frame.

Figure 62: (right) Normalized comparative plots (to area = 5000) of the signal MC simulation and "scaled" background simulation of the thrust magnitude. These are taken in the photon recoil frame.

9 Characterization of Reconstructions

9.1 Efficiency

Consider the efficiency distribution of the signal decay with cuts. Below we have plotted the following quantities: 1) the reconstructed cosine helicity angle, suitably background-subtracted, 2) the generator-level cosine helicity angle for all events which pass the cuts, and 3) the generator-level cosine helicity angle for all 10,000 events. We plot for maximal parity violation ($T_1 = T_2$, c.f. equation 20) and minimal parity violation ($T_1 = 0$).

Furthermore, efficiency plots for parity conservation and parity violation are fit to the cosine helicity angle function (see equation 31). Fitted error plots are shown below, in figures 67 and 68. Note that, in figure 67, the efficiency distribution is symmetric about $\cos\theta = 0$ – there is no parity violation in the selection criteria. For the case of maximal parity violation, the efficiency distribution is asymmetric.

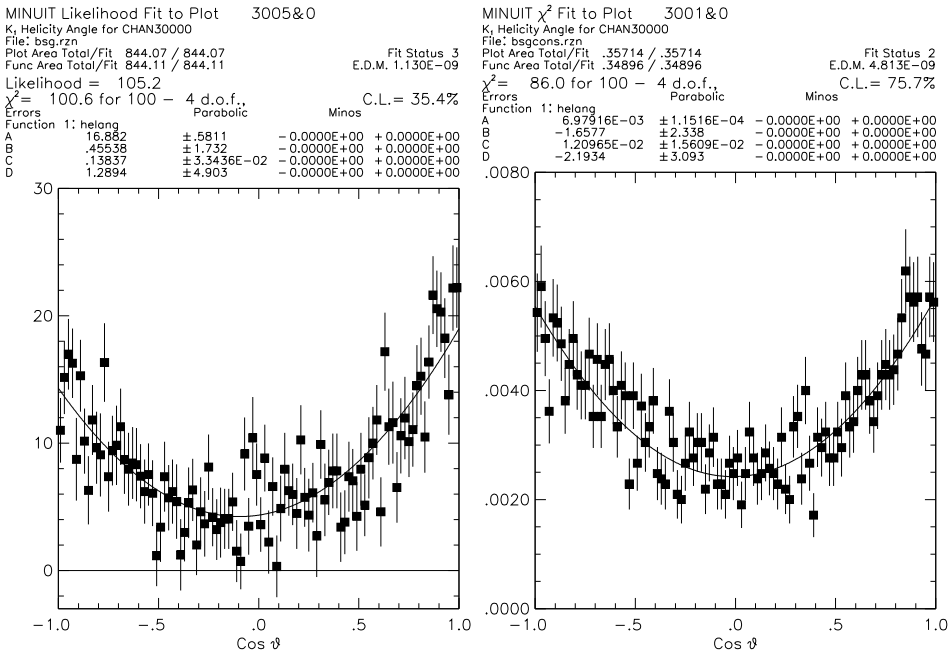

Figure 63: (left) Plot of the sideband-subtracted cosine helicity angle, for 10,000 events. Here, the expectation value is $\langle \cos\theta \rangle = -0.1383 \pm 0.0334$.

Figure 64: (right) Plot of the reconstructed cosine helicity angle, without sideband subtraction, for 10,000 events. Here $\langle \cos\theta \rangle = -0.0835 \pm 0.0154$.

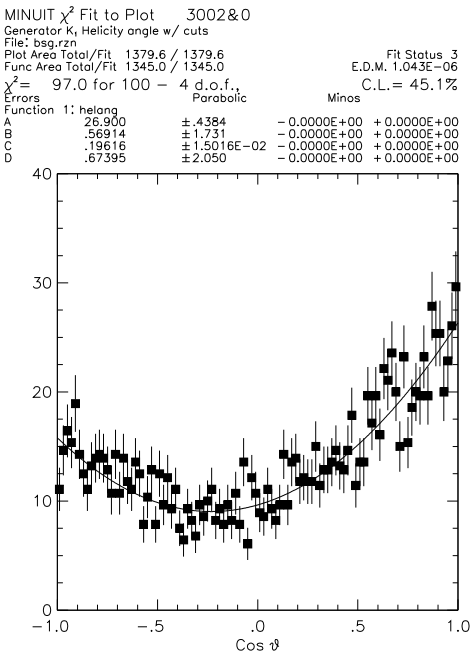

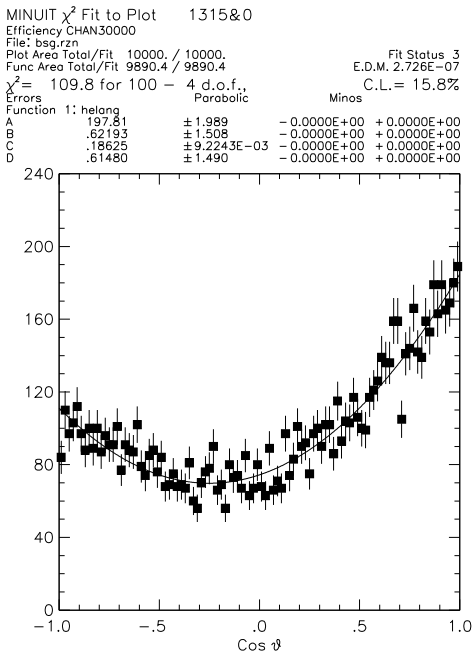

Figure 65: (left) Plot of the generator-level cosine helicity angle distribution for all events which pass the cuts. Here, the expectation value is $\langle \cos\theta \rangle = -0.1962 \pm 0.0151$. The expectation value shown here is statistically different from that of the reconstructed expectation value.

Figure 66: (right) Plot of the generator-level cosine helicity angle for all events. Here, the expectation value is $\langle \cos\theta \rangle = -0.1865 \pm 0.0092$.

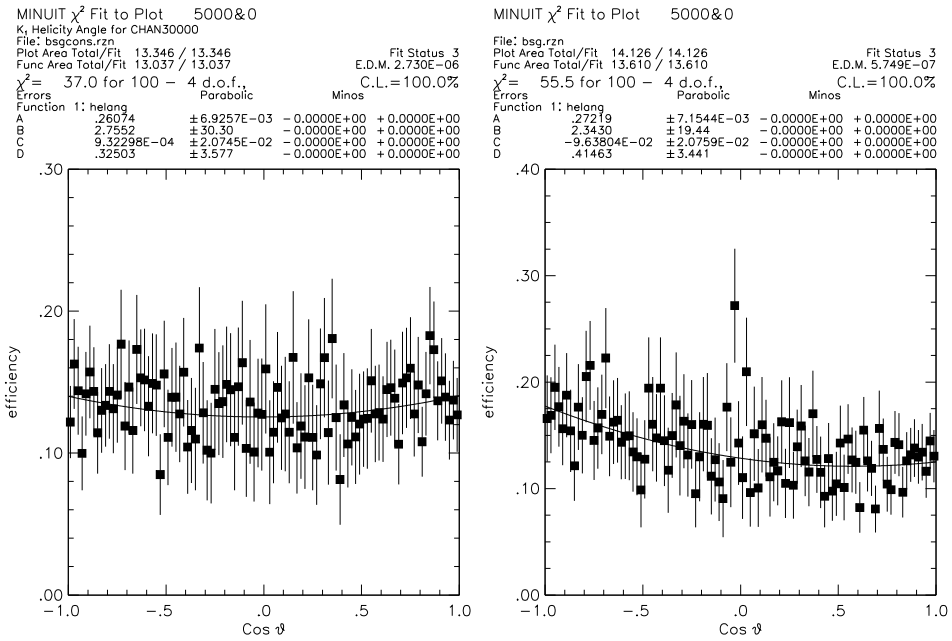

Figure 67: (left) Efficiency distribution, as a function of cosine helicity angle, for the case of parity conservation. Here, as shown in the fit, we get a symmetric distribution.

Figure 68: (right) Efficiency distribution, as a function of cosine helicity angle, for the case of maximal parity violation. We have a large linear term, due largely to the fact that the expectation values of generator and reconstruction cosine helicity angles are different (see figures 76 and 79 for comparison).

9.2 Resolution

A further measure of the efficacy of reconstruction is to determine whether there is any systematic bias between the generator level measured observable and that observable determined from the reconstruction. To control bin migration, we construct a symmetric bin distribution, where $-1.0 < \cos\theta_{gen} - \cos\theta_{rec} < 1.0$; this is done with an odd number of bins, say 101. We fit this distribution to the following gaussian:

$$n(x) = \frac{N_0}{\sqrt{2\pi}\sigma} e^{-(x-\mu)^2/2\sigma^2} \tag{47}$$

we find that the mean and standard deviation are given by the following:

$$\hat{\mu} = -2.31 \pm 2.33 \times 10^{-4} \tag{48}$$

$$\hat{\sigma} = 1.12 \times 10^{-2} \pm 1.69 \times 10^{-4} \tag{49}$$

The mean is not statistically different from zero; thus, we may conclude that there is neither systematic bias between the generator level cosine helicity angle and the reconstructed cosine helicity angle.

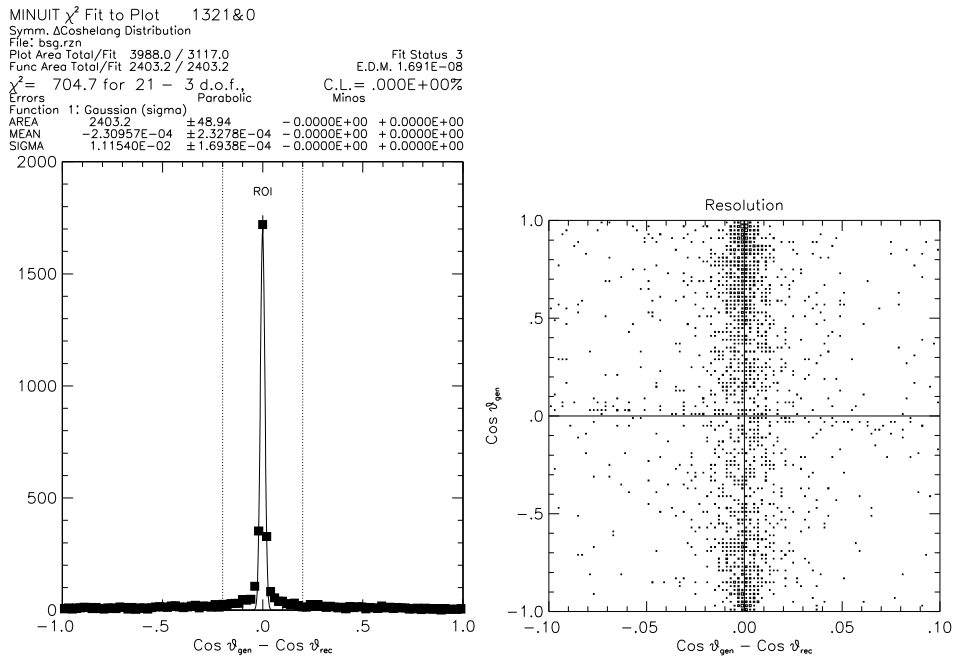

Figure 69: (left) Plot of the symmetric distribution of $\cos\theta_{gen} - \cos\theta_{rec}$ for the signal decay. Here, out of 3920 events, 1708 lie within the first bin ($|\Delta\cos\theta| < 9.9 \times 10^{-3}$). We fit the distribution to a Gaussian using χ^2 minimization, and excluding all points such that $|\cos\theta_{gen} - \cos\theta_{rec}| \geq 0.2$.

Figure 70: (right) Resolution as a function of the actual particle ID-level cosine helicity angle; on the horizontal axis lies the actual cosine helicity angle, $\cos\theta_{gen}$, while on the vertical axis lies the difference with the background-subtracted cosine helicity angle, $\cos\theta_{gen} - \cos\theta_{rec}$.

In any case, even assuming the most optimistic results in the above, with maximal parity violation and large (> 1000) samples, any expected systematic bias will be only one standard deviation in difference in the parity-violating effect. In other words, although there may be a statistical bias, this bias ($\approx 10^{-2}$) should not significantly affect the data.

10 Background Subtraction

10.1 No Event Shape Variable Cuts With Continuum Background Rescaling

The number of events for the "background" and "signal are given by the following simple functional forms:

$$\mathcal{N}_{bkgnd} = \frac{N_{bkgnd}}{N_{tot}} \times \mathcal{L} \times \sigma_{q\overline{q}} \tag{50}$$

$$\begin{aligned} \mathcal{N}_{signal} &= \mathcal{L} \times \sigma_{B\overline{B}} \times 2 \times \frac{1}{2} \times \mathcal{B}(B \to \gamma K\pi\pi) \times \epsilon(B \to \gamma K\pi\pi) \\ &= \frac{N_{signal,B\overline{B}}}{N_{tot}} \times \mathcal{L} \times \sigma_{B\overline{B}} \end{aligned} \tag{51}$$

Here, the cross-section for $B\overline{B}$ production is $\sigma_{B\overline{B}} = 1.07$ nb, and for the $q\overline{q}$ continuum background it is $\sigma_{q\overline{q}} = 3.1$ nb. Furthermore, in equation 51 we multiply by 2 because of B pair production, and divide by 2 in order to discount the charged modes of the B. Furthermore, in the context of this paper we consider only the B decay mode $B, \overline{B} \to \gamma K^{\pm}\pi^{\mp}\pi^0$. Each of the 6 possible decay modes has a branching fraction of $\approx 10^{-5}$ and an efficiency, with the above cuts, of $\approx 13\%$.

For the background, we note that the signal region (see figure 47) corresponds to the following, for the reconstructed modes: -0.2 GeV $< \Delta E < 0.2$ GeV and 5.27 GeV $< M_{beam} <$ 5.29 GeV, and passing other kinematic and combinatoric cuts on the decay. Using off-resonance on the Monte Carlo background we have that the center-of-mass energy is 10.56 GeV; thus, the energy of the reconstructed B meson is 5.2625 GeV (see figures 71). A relatively simple way to compensate for this lower, off-resonance energy (Υ_{4S} resonance is located at 10.58 GeV) is to scale the momenta of the particles by 5.29/5.2625, and also to change the beam energy to this corresponding amount. We keep all the cuts and keep the calculated invariant masses the same, but to change the momenta and the energies of the "scaled" particles.

$$E'_{beam} = \frac{5.29}{5.2625} E_{beam} \tag{52}$$

$$\mathbf{p}' = \frac{5.29}{5.2625} \mathbf{p} \tag{53}$$

$$E' = \sqrt{m_0^2 + \mathbf{p}'^2} \tag{54}$$

First, however, we need only compare to the following case – the background decay in which the center-of-mass energy is 10.58 GeV, to the case where the continuum background has a center-of-mass energy of 10.53 GeV.

An event is considered to be in the signal if the combination passes the kinematic cuts. As in the case of signal decays, we consider only the "best" combination of four particles – that combination which is closest to the B mass. From the above, we see the following in terms of $\mathcal{L}$, the luminosity of the CESR collider. Here, b1 refers to a Monte Carlo simulation of the $q\overline{q}$ background generated at resonance $E_{cm} = 10.58$ GeV; b2 refers to the Monte Carlo simulation of the $q\overline{q}$ continuum background generated off resonance at $E_{cm} = 10.56$ GeV. The combinatoric cut is that the decay $B^0, \overline{B^0} \rightarrow \gamma K^{\pm}\pi^{\mp}\pi^0$ occurs (or is seen). These numbers are taken for a 100,000 event run.

As a confirmation that the "scaled" off-resonance continuum background is somewhat correct is the fact that the maximum beam constrained mass is $10.58/2 = 5.29$ GeV, for both the "scaled" continuum background and the hypothetical continuum background at 10.28 GeV.

$$N_{signal,b2} = 151 \pm \sqrt{151} = 151 \pm 12.2 \tag{55}$$

$$N_{signal,b1} = 114 \pm \sqrt{215} = 114 \pm 10.7 \tag{56}$$

The discrepancy will be treated as a contribution to our systematic error;

thus, we may use the following as the determination of the number of events due to the background, as the "renormalized" background with center-of-mass energy 10.58 GeV (i.e. b1). Now, with this calculate (in terms of $\mathcal{L}$) the number of signal events of this particular decay that we should see, using equations 50 and 51:

$$\mathcal{N}_{bkgnd} = \frac{N_{signal}}{N_{tot}} = 4.681 \times 10^{-3}\mathcal{L} - nb \tag{57}$$

$$\mathcal{N}_{signal} = 3.857 \times 10^{-6}\mathcal{L} - nb \tag{58}$$

Therefore the noise-to-signal ratio here is 1214 to 1! Therefore, we need extremely sharp cuts to suppress the continuum backgrounds.

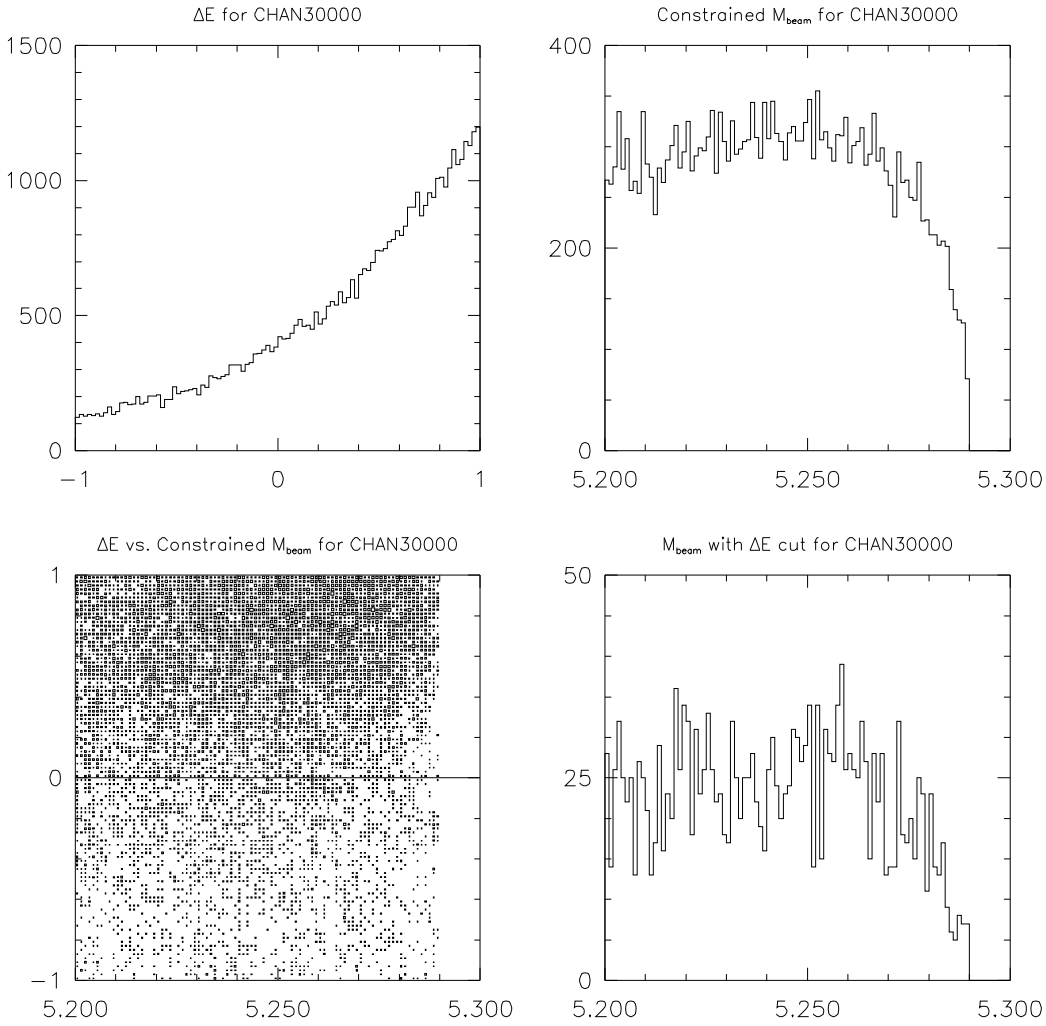

Figure 71: Plots of kinematic variables M_{beam} and ΔE for the "scaled" off-resonance continuum background decay, where $E_{cm} = 10.56$ GeV; note that although we choose the "best" combination as those particles which come closest to the invariant B mass, there does not appear to be a pronounced peak (i.e. negligible mass bias) at the B mass. In any case, this bias in the continuum background will not affect the observation of the signal, as the simulated background contains no signal B decay.

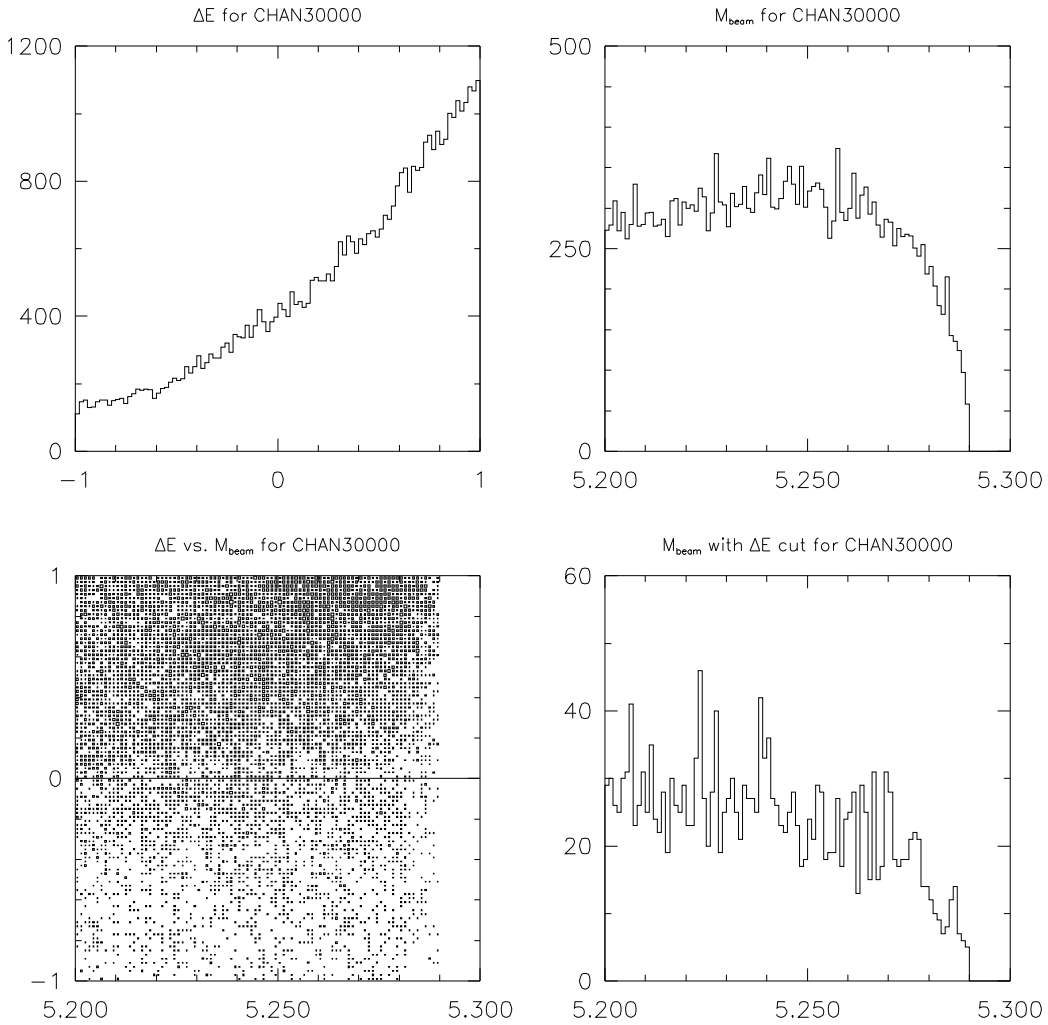

Figure 72: Plots of kinematic variables M_{beam} and ΔE for the "unscaled" resonance continuum background decay, where $E_{cm} = 10.58$ GeV; note that although we choose the "best" combination as those particles which come closest to the invariant B mass, there does not appear to be a pronounced peak at the B mass. In any case, this bias in the continuum background will not affect the observation of the signal, as the simulated background contains no signal B decay. Furthermore, these kinematic plots are identical to the scaled continuum background set at $E_{cm} = 10.53$ GeV.

10.2 Scattering Angles

A further cut we may make is the angle our reconstructed candidate B makes with the beam axis. Continuum background events are events of the form $e^+e^- \to q\overline{q}$, or events where the initial and final states are two fermions. However, signal events are of the form $e^+e^- \to \Upsilon_{4s} \to B\overline{B}$, or events in which the initial state is two fermions and the final state is two bosons. A convenient measure of differential cross section is an axis along the momenta of the electrons; the differential cross section for continuum background events (per unit solid angle) is independent of angle, wherease the differential cross section for $B\overline{B}$ events is proportional to $\sin^2\theta$. See figures 74 and 75 for these relations. Here, due to the efficiency of cuts made on the event shape

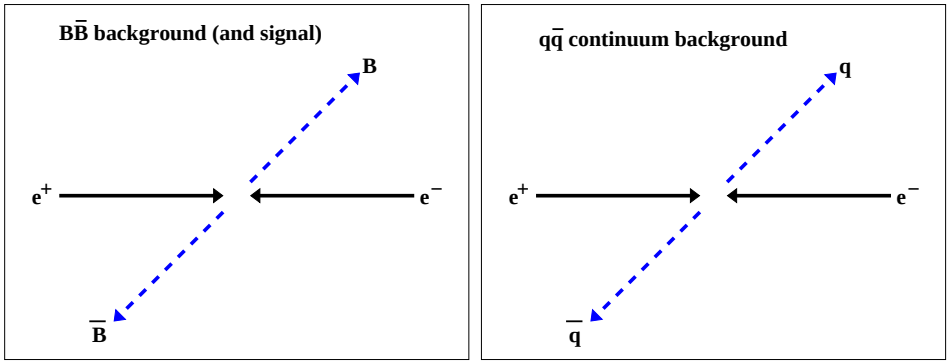

Figure 73: The two main types of collisions that may occur near the Υ_{4s} resonance about 10.58 GeV. As shown, these two events are continuum background events and $B\overline{B}$. We take the z-axis to be along the beam, coincident with the momentum axis of the electron and positron.

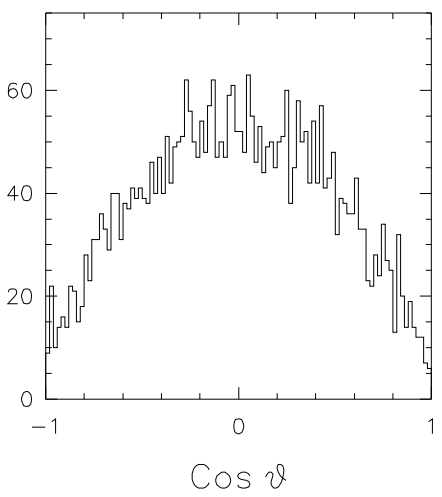

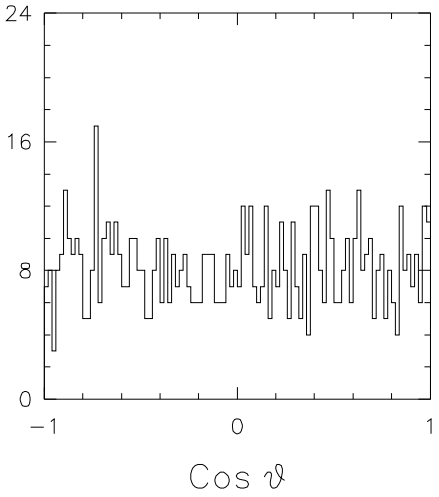

Figure 74: (left) Plot of the angle made by the reconstructed candidate B meson, for a Monte Carlo simulating signal events. Here, the differential cross section $\frac{d\sigma}{d\Omega} \propto \sin^2\theta_z$.

Figure 75: (right) Plot of the angle made by the reconstructed candidate B meson, for a Monte Carlo simulating $q\overline{q}$ continuum events. Here, the differential cross section $\frac{d\sigma}{d\Omega}$ is isotropic.

variables (see figures 61 and 56), we need not make a relatively inefficient cut on this scattering angle.

10.3 Final Background Subtraction Results

When we ran 10^6 events in off-resonance continuum background decays, we saw $N_{q\overline{q}} = 882 \pm 29.7$; the simulation of signal events we expect to see was encoded by "bb_4s3.ctr," which encodes for the Υ_{4s} triplet state, where

$\Upsilon \to B\overline{B}$. From this, we see the following:

$$N_{bkgnd} = 16 \pm 4.0 \tag{59}$$

$$N_{signal} = 25 \pm 5.0 \tag{60}$$

Therefore, using equations 50 and 51, we get the following measures of the number of events we should see, as well as a signal to noise ratio:

$$\mathcal{N}_{bkgnd} = \frac{N_{signal}}{N_{tot}} \times \mathcal{L} \times \sigma_{q\overline{q}} = 4.96 \times 10^{-5} \pm 1.24 \times 10^{-5} \mathcal{L} - \text{nb} \tag{61}$$

$$\mathcal{N}_{signal} = \frac{N_{signal,B\overline{B}}}{N_{tot}} \times \mathcal{L} \times \sigma_{B\overline{B}} = 2.68 \pm 0.54 \times 10^{-5} \mathcal{L} - \text{nb} \tag{62}$$

Thus we have a signal-to-background (or "noise") ratio of 1.9 ± 0.6 to 1. Although the background is higher than the background, however we may still determine the level of signal, with the above cuts, since the signal level is not smaller than the level of statistical fluctuations in background.

The luminosity of the CESR collider, under operation of the CLEO III detector is at a maximum of $\approx 6 \times 10^{33} \text{cm}^{-2}\text{s}^{-1} = 6\text{nb}^{-1}\text{s}^{-1}$. Therefore, at the highest level of operation, we should get these absolute levels with the

cuts given above:

$$\mathcal{N}_{bkgnd} = 2.98 \pm 0.74 \times 10^{-4} \text{ s}^{-1} \tag{63}$$

$$\mathcal{N}_{signal} = 1.61 \pm 0.32 \times 10^{-4} \text{ s}^{-1} \tag{64}$$

11 Final Thesis Results

Here, we have the following trends with respect to the parity-violating parameters shown here. In fact, below we have the trends with respect to the following variables: 1) the sideband-subtracted reconstructed cosine helicity angle distribution, 2) the cosine helicity angle distribution for generator-level data for all events which pass the signal cuts, and 3) the generator-level data. The following are shown below, in figures 76, 77, and 78. However, note that there is a great deal of variation for the parity-violating trend for the background-subtracted reconstruction; a plot of the cosine helicity angle without background subtraction yields the following, where we have not rescaled the errors in the observable to 10,000 events – rather, we have used the error for the the given sample size, i.e. the sample size of events in the signal region. Furthermore, we note that give a reconstruction of magnitude scaled to 1, of which $\alpha < 1$ consists of a parity-conserving "reconstruction" background with a flat $\cos\theta$ distribution, that the total distribution can be represented as the following, where $x = \cos\theta$ (see equation 31 for an analo-

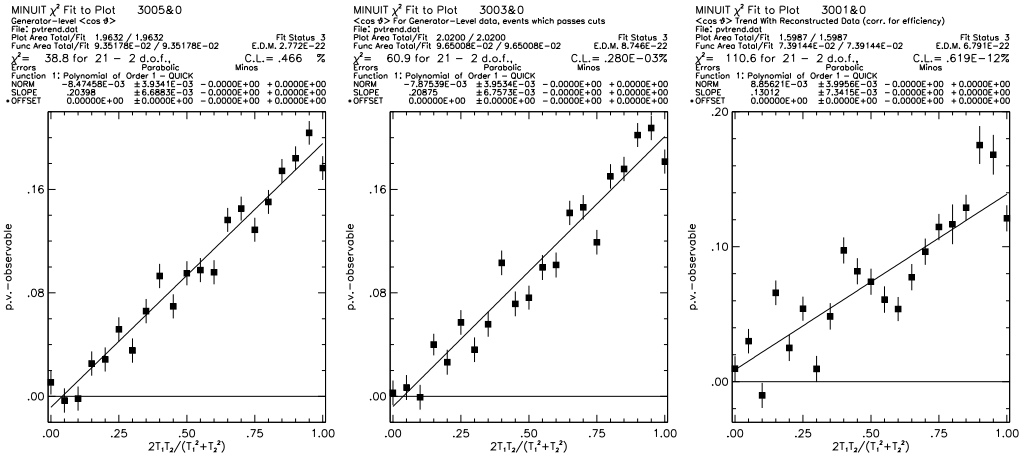

Figure 76: (left) Plot of the trend in the parity violating observable, as a function of the parity-violating parameter $q = 2T_1T_2/(T_1^2 + T_2^2$. Here, we see that the parity-violating observable y has the following trend: $y = \alpha q + \beta$, where $\alpha = 0.2040 \pm 0.007, \beta = -0.0087 \pm 0.0039$.

Figure 77: (middle) Plot of the trend in the parity-violating observable, as a function of the parity-violating parameter, for generator-level data in which the events pass all the cuts. Here, we see that in the fit $y = \alpha q + \beta$, $\alpha = 0.2088 \pm 0.0068, \beta = -0.0079 \pm 0.0039$.

Figure 78: (right) Here is a plot of the parity-violating trend for sideband-subtracted reconstructed events. Here, we have the following $\alpha = 0.1301 \pm 0.0073, \beta = 0.0086 \pm 0.0040$. In addition, the variation using sideband subtraction is extreme.

gous equation):

$$n_{tot}(x) = \frac{a}{2a + 2/3c} + bx + \frac{c}{2a + 2/3c}x^2 \tag{65}$$

The expectation value for this distribution is then $\langle x \rangle_{n_{tot}} = b$. However, if we subtract out this level of background, such that we have a distribution

approaching that of the cosine helicity angle distribution, then:

$$n'(x) = \frac{a}{2a + 2/3c} + bx + \frac{c}{2a + 2/3c}x^2 - \frac{\alpha}{2} \tag{66}$$

Here, the expectation value using this distribution is:

$$\langle x \rangle_{n'} = \frac{\int_{-1}^{1} x n'(x)\, dx}{n'(x)\, dx} \tag{67}$$

$$\langle x \rangle_{n'} = \frac{b}{1 - \alpha} \tag{68}$$

Thus, if we subtract a background of level $\alpha < 1$, then we will get a substantially different distribution. However, as shown in figure 80, we cannot make any generalizations of the data using this method, as even for relatively large values of the parity-violating parameter, we still get very large variation about a "mean" level of generator level to reconstruction observables. The efficiencies of the sideband-subtracted reconstructions are ≈ 0.09. The efficiencies of the generator-level events which pass all the cuts are ≈ 0.13. These flat plots are shown in figures 81 and 82. From the data here, for 10,000 events we have an efficiency of 0.1359 ± 0.0033 and $\langle \cos\theta \rangle = 0.1133 \pm 0.0096$ (scaled to 10,000 reconstructed events).

12 Conclusions

Amazingly, the assumed branching ratio of $\approx 10^{-4}$ is implied, given an efficiency of 0.13 and an inferred 25 events out of 10^6 $B\overline{B}$ decays, which is at odds with the literature's estimate $\mathcal{B} \approx 10^{-5}$[4].

From the above relations, we see that the parity violating parameter, as expected, linearly tracks the parity violating observable. Furthermore, if we take the results of the $B\overline{B}$ Monte Carlo as a roughly accurate measure of the branching fraction, then we see that $\mathcal{B}(B^0, \overline{B^0} \rightarrow \gamma K^{\pm}\pi^{\mp}\pi^0) \approx 2.5 \pm 0.5 \times 10^{-5}$[4]. In CLEO III, we expect to see 60 million $B\overline{B}$ pairs and in CLEO II, we expect to see 10 million $B\overline{B}$ pairs; thus, considering the efficiency and the branching fraction, we should see the following number of candidate events:

$$N_{CLEOIII} = 1500 \pm 300 \tag{69}$$

$$N_{CLEOII} = 250 \pm 50 \tag{70}$$

Thus, we should see, at most, a 4.6σ effect for CLEO III, which is on the bare limits of distinguishability; for CLEO II, we should see only a 2.0σ effect. However, the high level of background, with these event shape variable cuts,

[4]simulated MC $B\overline{B}$ decays, resulted in 25 ± 5 events out of 10^6 which passed all the cuts to be considered a candidate B

should make it difficult, if not impossible, to resolve the signal. Fortunately, although there is a high level of $q\overline{q}$ continuum backgrounds, there is no correspondingly large $B\overline{B}$ backgrounds – the relatively high efficiency (before event shape variable cuts) of extracting this signal decay is due to π^0 veto.

13 Further Research

The focus of further research in this topic is in the form of more refined cuts that remove background without removing signal. These consist of *neural nets* which can be effective in strongly discriminating background. Simple linear neural nets can be used, as well as Fisher Discriminants, in order to remove the effects of backgrounds by a factor of 10^5 with less than 50% loss in signal decay; finally, after establishing cuts that are far more discriminating to the $q\overline{q}$ backgrounds, we may employ this analysis with the CLEO III data.

14 Acknowledgements

I would wish to thank Dr. Alan Weinstein for his impromptu lectures on particle physics, statistics, the CESR particle detector, my code, the Monte Carlo simulation, and everything in between, and his deep concern with both

my progress and understanding of the material; Dr. Mauritius Schmidtler and Anna Shapiro for helping me on anything, whether it be the idiosyncracies of FORTRAN or the eccentricities of the MN_FIT plotting program or the debugger; and certainly Dr. Jon Urheim, who showed me how to reconstruct the particle data and who always came by to see if I understood what I was doing. I thank you all for having the endurance to listen to my often repetitive questions.

References

[1] M. Kobayashi and C. Maskawa, *Prog. Theo. Phys.* **49**, 652 (1973).

[2] K. Hikasa *et. al.* (Particle Data Group), "Review of Particle Properties," Phys. Rev. **D45**, 1 (1992).

[3] "Resonance Structure of $\tau^- \to K^-\pi^+\pi^-\nu_\tau$ Decays", CLEO Collaboration (A. Anastassov *et. al.*), CONF 98-14 (1998); "Decays of Tau Leptons to Final States Containing K^0_S Mesons", CLEO Collaboration (T. Coan *et. al*), *Phys. Rev.* **D53**, 6037 (1996).

[4] See, *e.g.*, "Branching ratio and direct CP-violating rate asymmetry of the rare decays $B \to K^*\gamma$ and $B \to \rho\gamma$", C. Greub, H. SImma, D.

Wyler, DESY 94-089, hep-ph/9406421 (1994).

[5] "Determination of V-A dominance in B decays", S. Stone, CBX 91-77 (1991).

[6] *Phys. Rev. Lett.* **76**, 3898 (1996); Anders Ryd, UCSB thesis (1996); J. Stephen Miller, Caltech thesis (1998).

[7] See, for example, article by N.P. Deshpande in *B decays*, 2nd edition, S. Stone, ed., World Scientific, 1997.

[8] N.P. Deshpande, P. Lo, J. Trampetic, *Z. Phys* **C40**, 369 (1988).

[9] See *Review of Particle Physics, Eur. Phys. J.* **C3**, 1-794 (1998).

[10] "CP Asymmetry in $b \to s\gamma$", A. Lyon, J. Ernst, E. Thorndike, CBX-99-Rb (not yet distributed), 3/8/99.

[11] G.C. Fox and S. Wolfram, *Nucl. Phys.* **B149**, 413 (1979).

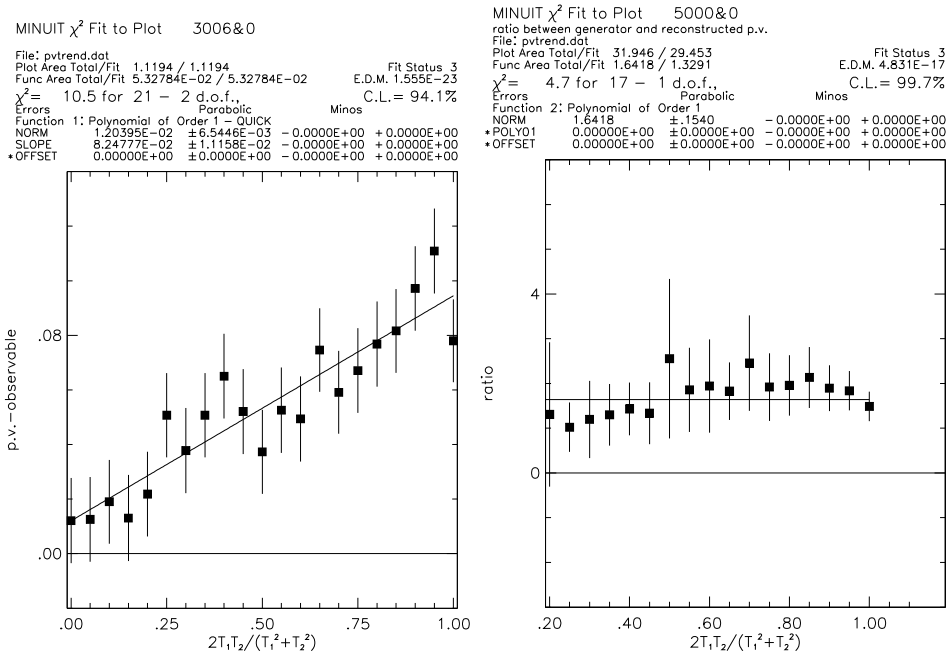

Figure 79: (left) Plot of the parity-violating trend for all reconstructed events in the signal region. Here, we have the following $\alpha = 0.0922 \pm 0.0111$ and $\beta = 0.0039 \pm 0.0065$. We make no rescaling to a sample size of 10,000 samples, as we have done in figures 76, 77, and 78.

Figure 80: (right) Here, we plot the ratio between the reconstructed cosine helicity angle distribution, without sideband subtraction, to that of the generator-level data. Here, we include only those values of the parity-violating parameter (i.e. $2T_1T_2/(T_1^2 + T_2^2) > 0.2$ in which the observable is statistically different from zero.

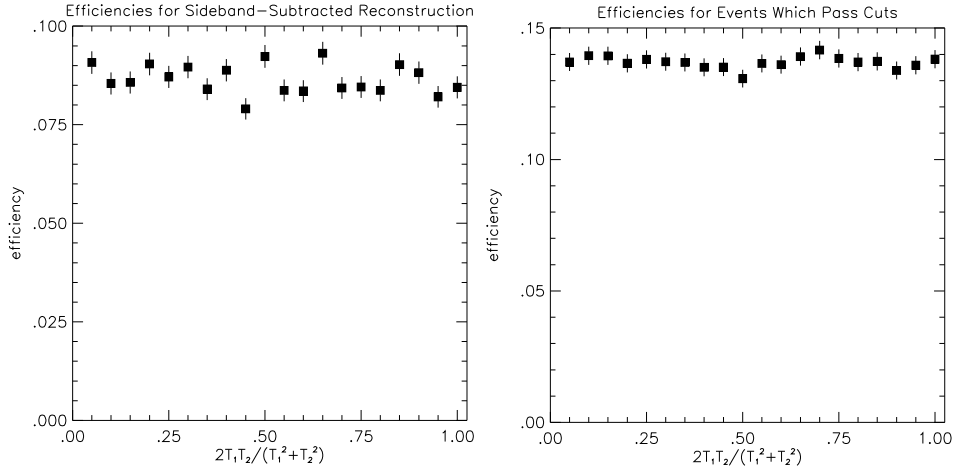

Figure 81: (left) Plot of the efficiency, as a function of parity-violating parameter (i.e. degree of parity violation), for sideband-subtracted reconstructed events, out of a simulated total 10,000 events.

Figure 82: (right) Plot of the efficiency, as a function of parity-violating parameter, for all events (signal and background within the signal) which pass all the cuts.